



Reclassification of four aubrites as enstatite chondrite impact melts: Potential geochemical analogs for Mercury

Arya UDRY ^{1*}, Zoë E. WILBUR^{1,2}, Rachel R. RAHIB¹, Francis M. McCUBBIN³, Kathleen E. VANDER KAADEN², Timothy J. McCOY ⁴, Karen ZIEGLER⁵, Juliane GROSS^{6,7}, Christopher DEFELICE¹, Logan COMBS¹, and Brent D. TURRIN⁶

¹Department of Geoscience, University of Nevada Las Vegas, Las Vegas, Nevada 89154, USA

²Jacobs-JETS Technology, NASA Johnson Space Center, Houston, Texas 77058, USA

³NASA Johnson Space Center, Mailcode XI2, 2101 NASA Parkway, Houston, Texas 77058, USA

⁴Department of Mineral Sciences, National Museum of Natural History, Smithsonian Institution, Washington, District of Columbia 20560, USA

⁵Department of Earth and Planetary Sciences, Institute of Meteoritics, University of New Mexico, Albuquerque, New Mexico 87131, USA

⁶Department of Earth and Planetary Science, Rutgers State University of New Jersey, Piscataway, New Jersey 08854, USA

⁷Department of Earth and Planetary Sciences, American Museum of Natural History, New York City, New York 10024, USA

*Corresponding author. E-mail: arya.udry@unlv.edu

(Received 06 July 2018; revision accepted 27 December 2018)

Abstract—We present petrologic and isotopic data on Northwest Africa (NWA) 4799, NWA 7809, NWA 7214, and NWA 11071 meteorites, which were previously classified as aubrites. These four meteorites contain between 31 and 56 vol% of equigranular, nearly endmember enstatite, Fe,Ni metal, plagioclase, terrestrial alteration products, and sulfides, such as troilite, niningerite, daubréelite, oldhamite, and caswellsilverite. The equigranular texture of the enstatite and the presence of the metal surrounding enstatite indicate that these rocks were not formed through igneous processes like the aubrites, but rather by impact processes. In addition, the presence of pre-terrestrially weathered metal (7.1–14 vol%), undifferentiated modal abundances compared to enstatite chondrites, presence of graphite, absence of diopside and forsterite, low Ti in troilite, and high Si in Fe,Ni metals suggest that these rocks formed through impact melting on chondritic and not aubritic parent bodies. Formation of these meteorites on a parent body with similar properties to the EHa enstatite chondrite parent body is suggested by their mineralogy. These parent bodies have undergone impact events from at least 4.5 Ga (NWA 11071) until at least 4.2 Ga (NWA 4799) according to ³⁹Ar-⁴⁰Ar ages, indicating that this region of the solar system was heavily bombarded early in its history. By comparing NWA enstatite chondrite impact melts to Mercury, we infer that they represent imperfect petrological analogs to this planet given their high metal abundances, but they could represent important geochemical analogs for the behavior and geochemical affinities of elements on Mercury. Furthermore, the enstatite chondrite impact melts represent an important petrological analog for understanding high-temperature processes and impact processes on Mercury, due to their similar mineralogies, Fe-metal-rich and FeO-poor silicate abundances, and low oxygen fugacity.

INTRODUCTION

Enstatite-rich meteorites are a unique group of meteorites that are believed to have all formed in the innermost region of the protoplanetary disk (Baedeker and Wasson 1975; Kallemeyn and Wasson 1986;

Shukolyukov and Lugmair 2004; Pignatale et al. 2016) and come from parent bodies that are characterized by exceptionally low oxygen fugacities (fO_2), ranging from ~2 to ~6 log units below the iron-wüstite (IW) buffer (e.g., Keil 1968, 2010). These meteorites include enstatite chondrites, aubrites (also known as enstatite

achondrites), and rocks produced from varying degrees of melting of enstatite chondrite (or enstatite chondrite-like) precursors, such as partial melt residues, enstatite chondrite impact melts, and enstatite chondrite impact melt-breccias (Keil 1968, 1989, 2007, 2010; Watters and Prinz 1979; Brett and Keil 1986; McCoy et al. 1995; Rubin and Scott 1997; Rubin et al. 1997; Lin and Kimura 1998; Lin and El Goresy 2002; Van Niekerk et al. 2014; Weyrauch et al. 2018). The highly reducing conditions present during the formation of the enstatite meteorites resulted in rocks that predominantly consist of nearly FeO-free enstatite, plagioclase, Si-bearing metal, and exotic sulfides. The mineral assemblages comprising the enstatite meteorites provide the opportunity to better understand the dominant geochemical processes present under significantly reducing formation conditions, as typically lithophile elements (e.g., Ti, Cr, Mn, and Na) can exhibit chalcophile behavior at low oxygen fugacities (McCubbin et al. 2012; Vander Kaaden et al. 2017; McCoy et al. 2018). In addition, investigation of members of the enstatite meteorite clan allow us to distinguish between the various parent bodies that formed and parent body processes that occurred under similar conditions, and likely in the same region of the solar system (Clayton et al. 1984). The highly reduced nature and mineralogy of enstatite-rich meteorites is similar to the fO_2 of Mercury estimated using data from the MERcury Surface, Space ENvironment, GEOchemistry, and Ranging (MESSENGER) spacecraft (McCubbin et al. 2012, 2017; Zolotov et al. 2013). Although we do not have any confirmed mercurian samples in our collections, based on their similar fO_2 and inferred mineralogies (McCubbin et al. 2017; Namur and Charlier 2017; Vander Kaaden et al. 2017; McCoy et al. 2018), enstatite-rich meteorites could represent potential mercurian analogs.

Aubrites are a rare group of meteorites (only 30 classified at the time of writing of this manuscript) that hold important implications for reducing magmatic systems in our solar system, and have also been suggested as a potential petrologic analog for rocks on Mercury (Burbine et al. 2002). Northwest Africa (NWA) 4799, NWA 7214, NWA 7809, and NWA 11071, four newly recovered meteorites, were initially characterized as aubrites (Meteoritical Bulletin Database #94). Beyond the initial characterization of the NWA meteorites, no detailed examination was done to investigate their origins and formations. Consequently, we carried out a detailed geochemical and petrologic examination of these meteorites. We present petrographic analysis, bulk rock compositions, oxygen isotope compositions, and ^{39}Ar - ^{40}Ar ages of the four NWA samples to further constrain the processes responsible for their formation, as well as their parent bodies. Our data indicate that all four

meteorites are more akin to enstatite chondrite impact melts, such as Ilafegh 009, rather than aubrites based on prior studies of both meteorite groups (Keil 1968; Watters and Prinz 1979; Brett and Keil 1986; Bischoff et al. 1992; McCoy et al. 1995; Lin and Kimura 1998; Lin and El Goresy 2002). Although aubrites and enstatite chondrite impact melts both formed from melting processes, aubrites formed as a result of incipient melting due to radioactive heating, while the source of heating for impact melt rocks is linked to collisions. Given the similarities between enstatite chondrite impact melts and aubrites, we also assess the utility of enstatite chondrite impact melts as mercurian analogs.

SAMPLES AND ANALYTICAL TECHNIQUES

Samples

We have acquired one chip for each sample, and we investigated two thin sections for NWA 4799, NWA 7214, and NWA 11071, and one thin section for NWA 7809 (referred to as “the NWA meteorites” throughout this manuscript). Eighty-six pieces, totaling 365 g, of NWA 4799 were found in Algeria in 2007. A 2.2 kg stone of NWA 7214 was found in Western Sahara in 2010. A single stone of NWA 7809, with a mass of 230 g and several pieces of NWA 11071 for a total mass of 23.8 g, were found in an unknown location.

Electron Probe Microanalysis

Mineral major and minor element compositions of silicate, sulfide, phosphide, and metal phases within the four investigated meteorite samples were measured using the JEOL JXA-8900 electron microprobe (EMP) at University of Nevada, Las Vegas (UNLV) and the JEOL JXA-8530F EMP at the Johnson Space Center (JSC). Using the UNLV EMP, conditions of 15 keV and 10 nA were used for the silicates, and conditions of 20 keV and 20 nA were used for the sulfide, metal, and phosphide phases. The ZAF correction method was applied to all analyses. For the JSC EMP, conditions of 15 keV, 15 nA, and a PRZ correction were used for the silicates, and conditions of 15 keV, 20 nA, and a ZAF correction were used for the sulfide, metal, and phosphide phases. All phases were analyzed with a spot size of 5 μm . The following standards were used for EMP analyses of silicate phases at UNLV: augite (for analysis of Mg, Si), microcline (K), ilmenite (Ti, Mn, Fe), albite (Na), plagioclase (Al, Ca), pyrite (Fe, S), apatite (P), BaF_2 (F), AgCl (Cl), and chromite (Cr). The standards for sulfides were: augite (Mg, Si), CaF_2 (Ca), albite (Na), apatite (P), orthoclase (K), chromite (Cr), ilmenite (Mn), TiO_2 (Ti), pyrite (Fe, S), Co metal (Co), As (As), CuFeS_2 (Cu), and

Ni metal (Ni). For silicate analyses, peak count times of 60 s and background count times of 30 s were used for the major and minor elements, with the exception of Na, which had counting times of 10 s for peaks and 5 s for backgrounds. For sulfide analyses, peak count times of 30 s and background count times of 15 s were used for major and minor elements, with the exception of Na, which had counting times of 20 s for peaks and 10 s for backgrounds. The following information outlines the EMP standards used at JSC. The feldspar standards are: albite (for analysis of Si, Al, Na), orthoclase (Si, Al, K), anorthite (Si, Al, Ca), rutile (Ti), olivine (Fe, Mg), chromite (Cr), and rhodonite (Mn). For pyroxenes and olivines, the standards used were: olivine (Mg, Si, Fe), rhodonite (Mn), rutile (Ti), anorthite (Al), diopside (Ca), apatite (P), orthoclase (K), Ni metal (Ni), and tugtupite (Cl). The sulfides were standardized using: tugtupite (Cl), rutile (Ti), albite (Na), olivine (Mg), silicon metal (Si), apatite (P, Ca), orthoclase (K), troilite (S), chromite (Cr), rhodonite (Mn), Zn metal (Zn), Fe metal (Fe), and Ni metal (Ni). For silicate analyses, peak count times of 60 s and background count times of 30 s were used for Cl, Ti, Na, K, Cr, Mn, Fe, and Ni. Peak count times of 30 s and background count times of 15 s were used for Mg, Ca, and Si. Peak count times of 40 s and background count times of 20 s were used for P, S, Zn, and Al. For sulfide, phosphide, and metal analyses, peak count times of 40 s and background count times of 20 s were used for Cl, Ti, Si, P, Cr, and Mn. Peak count times of 60 s and background count times of 30 s were used for Na, Ni, and K, whereas peak count times of 30 s and background count times of 15 s were used for Mg, S, Ca, and Fe. The detection limits for all elements in the different phases are included in Table S1 in supporting information. Modal abundances (vol%) were obtained using ImageJ software, and employing pixel count analyses of Mg, Fe, Ca, Al, Si, Cr, S, Na, Ti, Ni, and P X-ray maps, which were obtained by the JEOL JXA-8900 EMP at UNLV. The X-ray elemental maps were collected at 15 keV and 50 nA. We estimate an error of ~5% similar to Maloy and Treiman (2007) for the modal abundance determinations by supervised image classification technique.

Inductively Coupled Plasma–Mass Spectrometer (ICP-MS)

Bulk major and trace element abundances were determined with a Thermo Scientific iCAP Qc quadrupole ICP-MS at UNLV. About 50–100 mg of sample was dissolved in acid cleaned Savillex beakers in a 1:1 mixture of sub-boiled double distilled HNO₃ and Optima grade HF. Samples were diluted by a factor of about 5000 using ultrapure Millipore water (18.2 mega Ω). Samples were prepared with rock standards

BHVO-1, BHVO-2, BCR-1, and AGV-1, as well as total procedural blanks. Reproducibility of the reference materials was generally better than 5% (relative standard deviation—RSD). The same analytical sequence as Huang and Frey (2003) was followed and the same standard concentrations were used.

Laser Fluorination—Oxygen Isotope Analyses

Oxygen isotope analyses were performed by laser fluorination at the University of New Mexico Institute of Meteoritics (Sharp 1990). Three subsamples (~1–2 mg) were measured per sample. Samples were first leached by using 6N HCl in order to remove possible terrestrial weathering products. The filled Ni sample plate was placed in the vacuum chamber of the extraction line, pumped under high vacuum, and heated by an IR-lamp for a minimum of 12 hours in order to completely outgas the samples and remove potential moisture. Samples were then pre-fluorinated (BrF₅) in order to clean the stainless steel system and to react residual traces of water or air in the fluorination chamber. Molecular oxygen was released from the samples by laser-assisted fluorination (50 W infrared CO₂ laser) in a ~100 mb BrF₅-atmosphere, producing molecular O₂ gas, SiF₄ gas, and solid fluorides. Excess reagent and gaseous SiF₄ were separated from O₂ by reaction with hot NaCl and cryogenic trapping at –196 °C. The oxygen was purified by freezing onto a 13 Å molecular sieve at –196 °C, followed by elution of the O₂ from the first sieve at ~300 °C into a He-stream that carries the oxygen through a gas chromatography (GC) column (separation of O₂ and NF₃, a possible interference with the ¹⁷O measurement) to a second 13 Å molecular sieve at –196 °C. After removal of the He, the O₂ was then released directly into a dual inlet isotope ratio mass spectrometer (Thermo Finnigan MAT 253 Plus). The oxygen isotope ratios were calibrated against the isotopic composition of San Carlos olivine. Each sample analysis consists of 20 cycles of sample-standard comparison and olivine standards (~1–2 mg) were analyzed daily. Oxygen isotopic ratios were calculated using the following procedure: The $\delta^{18}\text{O}$ values refer to the per-mil deviation in a sample (¹⁸O/¹⁶O) from [standard mean ocean water (SMOW), expressed as $\delta^{18}\text{O} = (\frac{^{18}\text{O}}{^{16}\text{O}})_{\text{sample}} / [\frac{^{18}\text{O}}{^{16}\text{O}}]_{\text{SMOW}} - 1) \times 10^3$. The delta-values are converted to linearized values by calculating: $\delta^{18}\text{O}/^{17}\text{O}' = \ln[(\delta^{18}\text{O}/^{17}\text{O} + 103)/103] \times 103$ in order to create straight-line mass-fractionation curves. The $\Delta^{17}\text{O}'$ values were obtained from the linear δ -values by the following relationship: $\Delta^{17}\text{O}' = \delta^{17}\text{O}' - 0.528 \times \delta^{18}\text{O}'$, $\Delta^{17}\text{O}'$ values of zero define the terrestrial mass-fractionation line. $\Delta^{17}\text{O}'$ values lying on any line with a slope of ~0.52–0.53 are due to mass-dependent processes.

Typical analytical precision of the laser fluorination technique is better than $\pm 0.01\%$ for $\Delta^{17}\text{O}$.

Ar-Ar Method

We used $^{40}\text{Ar}/^{39}\text{Ar}$ step-heating method to evaluate the ages of crystallization of the four NWA meteorites. The step-heating method and the evaluation of the release spectra facilitates the examination of the ^{40}K (via the $^{39}\text{Ar}_{(\text{K})}$ proxy) and radiogenic ^{40}Ar distribution within the sample over the temperature range from ~ 500 °C to fusion (Turrin et al. 2008). In addition, the distribution of the apparent ages of the release spectra can also be evaluated relative to the atomic K/Ca ratios determined from the K and Ca proxies $^{39}\text{Ar}_{\text{K}}$ and $^{37}\text{Ar}_{\text{Ca}}$, respectively (see the release spectra in Fig. 8). In contrast, $^{40}\text{Ar}/^{39}\text{Ar}$ total fusion ages (integrated ages) do not yield this type of information, and thus can lead to difficulties interpreting the data.

The $^{40}\text{Ar}/^{39}\text{Ar}$ noble gas measurements were obtained at Rutgers University (RU) using custom built micro-noble gas extraction system (see Carr *et al.* [2007] for description) in line with an upgraded Mass Analyzer Product (MAP) 215–50 noble gas mass spectrometer with a digital ion-counting secondary electron multiplier (Turrin et al. 2010). All samples were loaded into a nominal 1.8 cm diameter Al-disk with 2 mm and 5 mm pits arranged in a controlled geometry together with the reference mineral standards Fish Canyon sanidine (FC-2), Hb3gr hornblende, and an internal blind laboratory sanidine standard (~ 315 Ma sanidine from a U-Pb dated tuff) that we use as to evaluate the neutron fluence (J). Samples were irradiated in the Cd-lined, in-core CLICIT facility of the Oregon State University TRIGA reactor for 80 hours. Values of J determined using 28.201 Ma (Kuiper et al. 2008) and 1080.4 Ma (Jourdan and Renne 2007) for the two standards range from 2.1186 to 2.1160×10^{-2} and produce an age within 0.2% of the U-Pb age of the internal standards. After irradiation, samples were heated incrementally using a 40 watt New Wave CO_2 laser system. A coaxial video camera with low resolution and a slightly off-axis two-color IR optical pyrometer was used to digitally image and record the step-heating process and the temperatures, respectively. The laser and sample chamber were connected to the rest of the sample extraction system without the need for a flexible connection, which significantly reduced the overall system volume, and hence lowers blanks. Typical static system blanks are (in 10^{18} mol): $^{40}\text{Ar} = 714 \pm 30$; $^{39}\text{Ar} = 13.3 \pm 1.0$; $^{38}\text{Ar} = 1.1 \pm 0.5$; $^{37}\text{Ar} = 24 \pm 0.2$; $^{36}\text{Ar} = 3.6 \pm 0.14$; we have determined that the blanks are independent of temperature. All errors are quoted at the 1- σ level of uncertainty.

RESULTS

Petrography

The reflected light images and composite X-ray maps of Fe, S, and Mg, as well as Mg, Al, and Si of the four samples are shown in Figs. 1–3, respectively. We present the modal abundances of the four samples in Table 1 and Fig. 4. Overall, the four enstatite chondrites show similar textures and modal abundances. We do not observe any relict chondrules, forsterite, or diopside in the seven investigated thin sections. In all samples, terrestrial alteration is present and mostly affects Fe, Ni metals and FeS. Ca-rich terrestrial weathering is also present in these rocks as veins (Table 1). For each sample, we have calculated the metal content present before terrestrial weathering using the method described in Van Niekerk et al. (2014), with the assumption that all weathering material is goethite (Table 1).

NWA 4799

Northwest Africa 4799 shows high degrees of terrestrial weathering (43–44 vol% terrestrial alteration products), with alteration products consisting of hydrated iron oxides that surround nearly all grains (Figs. 2 and 3). Alteration products also consist of altered metallic Fe, Ni veins, up to 1.1 mm in width, that crosscut both investigated thin sections. Alteration zones measure up to ~ 4 mm in width (typically red in Fig. 2). Northwest Africa 4799 does not include metal, but we calculated ~ 7.1 – 7.4 vol% of pre-weathering metal (Van Niekerk et al. 2014). This sample showing an igneous texture, consists of 40–41 vol% of fine- to medium-grained (up to 1.1 mm) euhedral to subhedral and striated enstatite grains and 14–16 vol% interstitial plagioclase up to 250 μm in length (Fig. 1a). Northwest Africa 4799 shows significantly lower abundances and a lesser diversity of sulfides compared to NWA 7214, NWA 7809, and NWA 11071. Anhedral minor daubréelite (FeCr_2S_4) measuring up to 200 μm in length and a single troilite (FeS) grain are the only sulfides observed in the studied sections. Graphite is also present in alteration veins. Bunch et al. (2008) previously reported observing kamacite [Fe, Ni metal], niningerite [MgS], perryite [(Ni, Fe) $_5$ (Si, P) $_3$], brezinaite [Cr_3S_4], and schreibersite [(Fe, Ni) $_3$ P] within NWA 4799; however, the two thin sections we have analyzed lack such minerals, likely due to biased sampling or terrestrial weathering.

NWA 7214

Northwest Africa 7214 is the least weathered sample in this study, with only ~ 2.7 – 3.5 vol% terrestrial weathering products in the two studied thin sections. This sample exhibits an equigranular igneous texture,

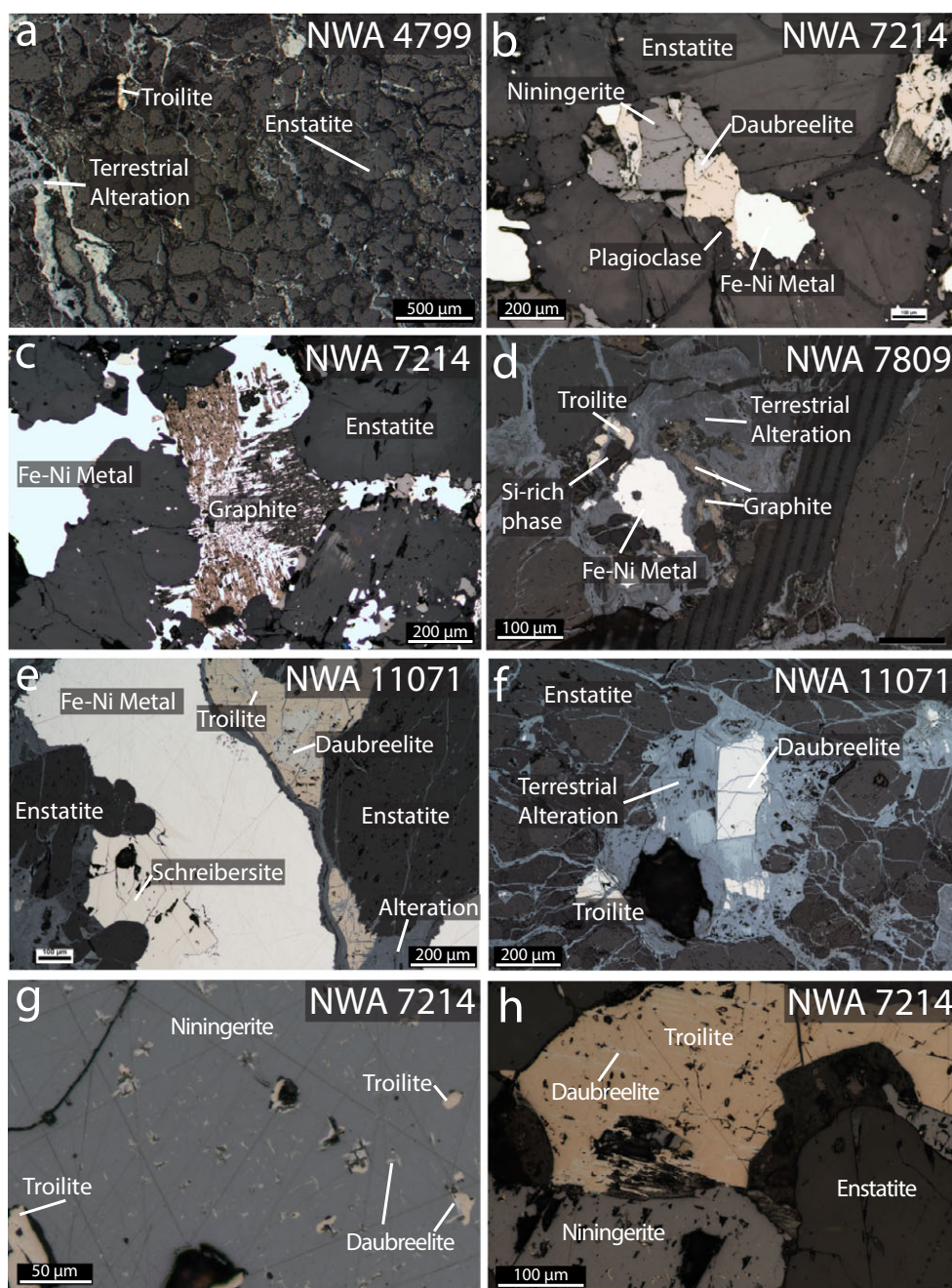


Fig. 1. Reflected light images of: a) NWA 4799: Euhedral-subhedral pyroxene with small troilite and terrestrial alteration of Fe,Ni metals. b) NWA 7214: Daubr elite exsolved from troilite and in contact with niningerite. c) NWA 7214: Graphite (bireflective in reflected light). d) NWA 7809: Fe,Ni metal, troilite, and graphite weathered by terrestrial alteration. e) NWA 11071: Schreibersite exsolved from Fe,Ni metal (low brightness image to distinguish schreibersite from metal). f) NWA 11071: Daubr elite surrounded by terrestrial alteration; troilite was likely completely weathered. g) NWA 7214: Niningerite with exsolution of troilite and daubr elite. The daubr elite grains might exsolved from troilite but it is not visible due to the 2-D nature of the thin section. h) NWA 7214: Troilite with daubr elite exsolutions. (Color figure can be viewed at wileyonlinelibrary.com.)

and consists of 63–67 vol% fine- to coarse-grained (200 μm to 4.5 mm) subhedral to euhedral, rounded, enstatite grains with 9.7–14.0 vol% interstitial plagioclase and 12–13 vol% metal (Fig. 1b). Round to

irregular metal grains averaging 600 μm in size are common throughout the sample. Schreibersite is observed within metal grains. About 1.6–1.9 vol% of large oldhamite [CaS] grains (up to 0.7 mm) are

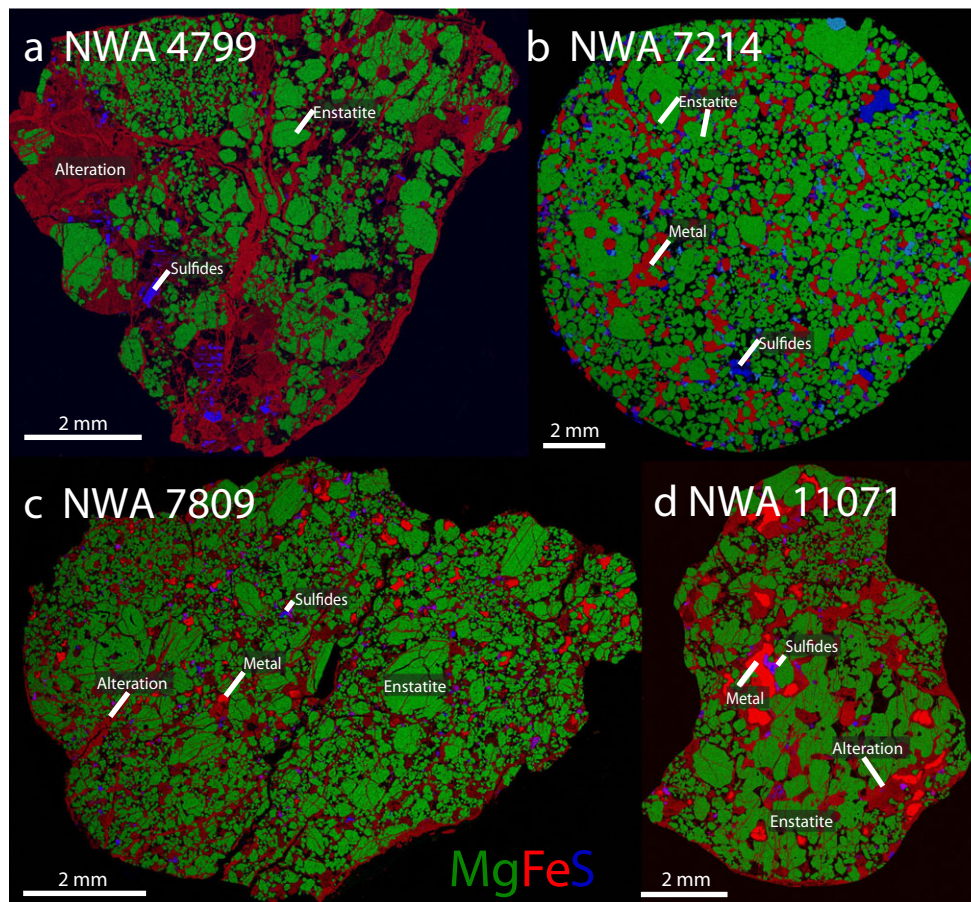


Fig. 2. Elemental composite maps of (a) NWA 4799, (b) NWA 7214, (c) NWA 7809, and (d) NWA 11071, including Fe (red), Mg (green), and S (blue). Green = enstatite; Dark red = terrestrial alteration; Bright red = Fe,Ni metal; Black = interstitial plagioclase; Light blue = niningerite, Purple = troilite and daubréelite; and Dark blue = oldhamite. The four meteorites have similar overall texture and different degrees of terrestrial alteration.

present, and both individual grains of troilite and niningerite are found within oldhamite grains. Minor daubréelite is present as an exsolution product of troilite (Fig. 1b). Niningerite is commonly associated with daubréelite (Fig. 1h). Some niningerite grains exhibit exsolution of both troilite and daubréelite (Fig. 1g). The daubréelite grains may have exsolved from troilite but it is not visible due to the 2-D nature of the thin section. Caswellsilverite [NaCrS₂] (up to 100 µm) is present on the margins of other sulfides. Graphite is also present, typically found near metal and sulfides, and less commonly found between silicates, or within silicates (Fig. 1c).

NWA 7809

Northwest Africa 7809 shows lower degrees of terrestrial weathering than NWA 4799 (31 vol% terrestrial weathering products) and contains 57 vol% of very fine- to coarse-grained (measuring up to 4.3 mm) euhedral to subhedral, rounded and elongate,

polysynthetically striated enstatite. NWA 7809 also contains 7.9 vol% interstitial plagioclase. Rounded to irregular metal grains (2.5 vol%) averaging 500 µm are found in association with graphite and schreibersite and 7.2 vol% of metal was likely present before weathering. Rare individual grains of daubréelite are observed, whereas individual grains of troilite including daubréelite exsolutions are more common. Both rounded and bladed grains of graphite, sometimes surrounded by terrestrial hydrated iron oxides, are observed in the studied thin sections (Fig. 1d).

NWA 11071

Northwest Africa 11071 shows lower degrees of terrestrial weathering than NWA 4799 (26–27 vol% terrestrial alteration products). Alteration pockets and alteration veins are observed, occasionally enclosing sulfide or metal grains. Subhedral, rounded, and elongated enstatite grains, measuring up to 2 mm, comprise 58–62 vol% of NWA 11071 (Figs. 1 and 2).

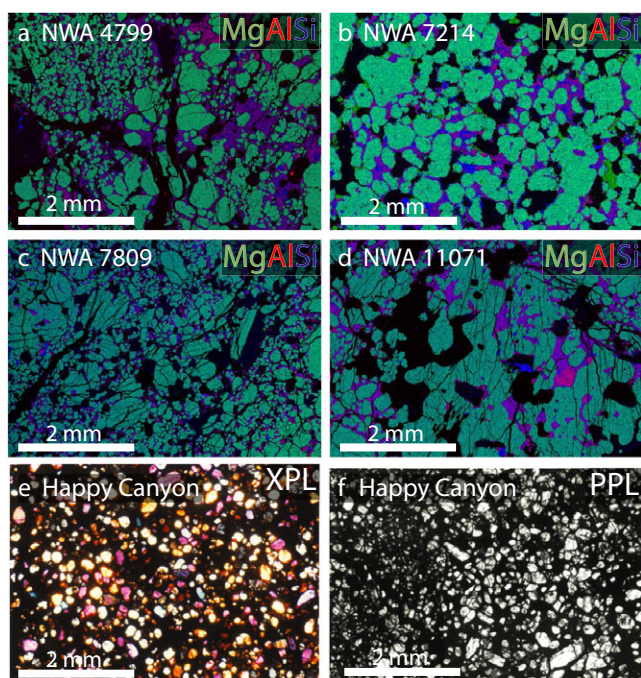


Fig. 3. Elemental composite maps of (a) NWA 4799, (b) NWA 7214, (c) NWA 7809, and (d) NWA 11071, including Al (red), Mg (green), and Si (blue) and (e) cross-polarized transmitted light image and (f) plane-polarized light image of Happy Canyon. All images are at the same scale. (Color figure can be viewed at wileyonlinelibrary.com.)

Interstitial plagioclase (7.1–11 vol%) is present and averages 400–500 μm in size. Schreibersite is observed within metal grains, and is typically found at metal boundaries (Fig. 1e). Metal is estimated to have been between 7.6 and 8.2 vol% of this sample before terrestrial alteration (Van Niekerk et al. 2014). Daubréelite lamellae are exsolved from troilite, and some rare individual daubréelite grains are present and are surrounded by terrestrial alteration (Fig. 1f).

Mineral Major Element Compositions

All mineral major element compositions are presented in Table S2 in supporting information.

Pyroxene

Pyroxene compositions are presented in Table 2. The predominant silicate phase in all four analyzed meteorites is FeO-poor enstatite. FeO concentrations within enstatite grains of the analyzed samples are <1 wt%, except for NWA 4799, which contains grains that have FeO concentrations of 1.1–1.8 wt%. Average FeO contents are 0.05 wt% (NWA 7214), 0.22 wt% (NWA 7809), 0.43 wt% (NWA 11071), and 0.58 wt% (NWA 4799). The average pyroxene compositions for NWA 4799, NWA 7214, NWA 7809, and NWA 11071

are $\text{En}_{98.3}\text{Fs}_{1.3}\text{Wo}_{0.4}$, $\text{En}_{99.4}\text{Fs}_{0.1}\text{Wo}_{0.5}$, $\text{En}_{98.9}\text{Fs}_{0.6}\text{Wo}_{0.4}$, and $\text{En}_{99.3}\text{Fs}_{0.2}\text{Wo}_{0.5}$, respectively. Average CaO pyroxene abundances are similar in the four NWA samples (from 0.16 wt% to 0.19 wt%).

Plagioclase

Plagioclase within all four samples show homogeneous albitic-rich compositions varying from $\text{An}_4\text{Ab}_{90}\text{Or}_6$ to $\text{An}_8\text{Ab}_{88}\text{Or}_4$, from NWA 7809 to NWA 4799, respectively (Table 3).

Fe,Ni Metal

Metallic Fe,Ni grains analyzed in NWA 7214, NWA 7809, and NWA 11071 are homogeneous and similar in composition (Table 4). The dominant Fe,Ni metal observed is low-Ni kamacite (average ~5.1 wt% Ni) that is Si-rich, with a range of 3.3–4.6 wt% Si. Northwest Africa 7214 contained metal with the highest Si content within the four studied meteorites, with 4.4–4.6 wt% Si. Two taenite grains were analyzed in NWA 11071, yielding compositions of ~25 wt% Ni. The Co content (0.43–0.50 wt%) in the four NWA meteorites is similar. Northwest Africa 4799 does not contain Fe,Ni metal, almost certainly as a result of terrestrial alteration.

Sulfides

See Table 5.

Daubréelite

Northwest Africa 4799, NWA 7809, and NWA 11071 contain zincian daubréelite (Zn >0.5 wt%), while NWA 7214 contains low abundances of Zn (Zn <0.07 wt%). NWA 4799, NWA 7809, and NWA 11071 have daubréelite Zn concentrations of 1.2–1.5 wt%, 1.8 wt%, 1.6–2 wt%, respectively. Northwest Africa 7214 daubréelite grains contain 0.03 wt% Zn.

Troilite

Troilite is observed in all four meteorites, and all contain both Cr and Ti. Northwest Africa 7809 and NWA 11071 grains have relatively homogeneous and similar Cr concentrations of 0.49–0.99 wt%. The troilite in NWA 7214 exhibited a large range of Cr abundances (0.54–5.7 wt%). The Ti content within NWA 7214 (1.2–1.6 wt%) is higher than that of NWA 7809 (0.06–1.10 wt%) and NWA 11071 (0.01–0.90 wt%). The only troilite grain in NWA 4799 contains 0.56 wt% Cr and 0.91 wt% Ti.

Niningerite

Northwest Africa 7214 is the only sample from this study, where niningerite is observed (Figs. 1a and 1b), which contains Ca (0.45–0.82 wt%), Na (0.12–0.48 wt%), and Cr (0.35–1.78 wt%) (Fig. 5). Neither alabandite nor keilite are observed in these meteorites.

Table 1. Mineral modal abundances (vol%) in the four NWA samples.

Meteorites	Enstatite	Feldspar	Metal	Fe-rich weathering products	Ca-rich weathering products	Pre-weathering metal*	Troilite	Ningerite	Daubréelite	Oldhamite	Caswellsilverite	Total sulfides	Total terrestrial weathering
NWA 4799 A	40	14	0.0	44	0.0	7.4	0.0	0.0	0.7	0.4	0.0	1.2	44
NWA 4799 B	41	16	0.0	43	0.0	7.1	0.0	0.0	0.4	0.0	0.0	0.4	43
NWA 7214 A	67	9.7	13	2.6	0.1	14	1.4	2.8	0.4	1.6	1.0	7.2	2.7
NWA 7214 B	63	14	12	3.3	0.2	13	1.4	3.0	0.4	1.9	1.1	7.7	3.5
NWA 7809	57	7.9	2.5	29	2.6	7.2	1.5	0.0	0.1	0.0	0.0	1.6	31
NWA 11071 A	62	7.1	3.5	24	1.3	7.6	1.4	0.0	0.2	0.0	0.0	1.7	26
NWA 11071 B	58	11	3.8	27	0.0	8.2	1.1	0.0	0.1	0.0	0.0	1.3	27

*Count Fe-rich weathering products (assumed to be goethite) of metal in vol%, and then correct the weathered metal abundance for volume and density differences between kamacite and goethite. This formula is $(\text{[weathered metal]/[6] + metal})$.

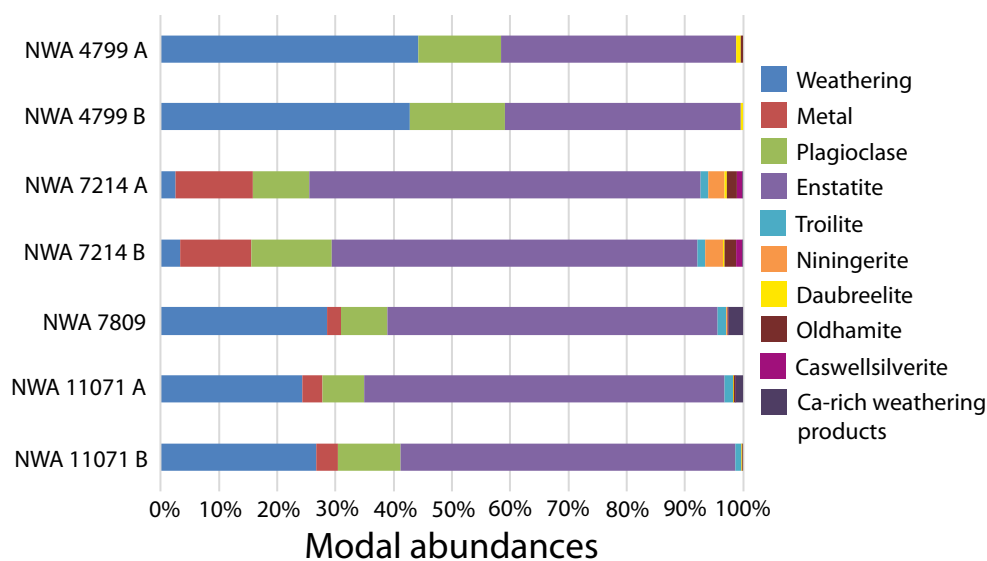


Fig. 4. Modal abundances for the seven studied thin sections for the four meteorites. Enstatite is the main mineral in the NWA samples with varying abundances of terrestrial alteration and metal.

Table 2. Average pyroxene compositions of the four studied meteorites.

wt%	NWA 4799		NWA 7214		NWA 7809		NWA 11071	
<i>n</i>	41	1 σ	37	1 σ	15	1 σ	27	1 σ
SiO ₂	58.9	0.4	59.1	0.30	59.0	0.35	59.1	0.4
Al ₂ O ₃	0.10	0.04	0.15	0.04	0.10	0.02	0.10	0.02
Cr ₂ O ₃	b.d.	b.d.	b.d.	b.d.	b.d.	b.d.	b.d.	b.d.
FeO	0.31	0.31	0.03	0.04	0.22	0.31	0.26	0.22
MgO	39.8	0.4	39.7	0.3	39.5	0.3	39.9	0.3
CaO	0.17	0.06	0.16	0.02	0.18	0.05	0.18	0.05
Total	99.3	1.2	99.1	0.7	99.1	1.0	99.5	1.0
En	99.3	0.1	99.7	0.1	99.4	0.4	99.3	0.3
Fs	0.44	0.43	0.04	0.05	0.32	0.44	0.37	0.30
Wo	0.30	0.10	0.29	0.03	0.32	0.09	0.33	0.09
Mg#	99.6	0.4	100.0	0.1	99.7	0.4	99.6	0.3

b.d. = below detection.

Oldhamite

Oldhamite observed in NWA 7214 contains Mg (0.98–1.67 wt%), Fe (0.12–0.91 wt%), and Mn (0.36–0.61 wt%).

Caswellsilverite

Caswellsilverite is only observed in NWA 7214 and contains Fe (0.09–2.00 wt%), Mn (0.06–0.20 wt%), and Ti (0.14–0.25 wt%).

Schreibersite

Schreibersite is observed in NWA 7214, NWA 7809, and NWA 11071. The grains in NWA 7809 and NWA 11071 have similar Ni content of 14.6–15.5 wt%, while schreibersite in NWA 7214 has lower Ni content of

11.0–12.1 wt% (Table S1). The Co and Si contents are nearly the same in all three meteorites (0.17–0.24 wt% Co, 0.22–0.35 wt% Si). Compositional gradients are not observed within individual grains.

Silica-Rich Phase

The four meteorite samples contain two types of Si-rich phases, which vary both compositionally and texturally. One high-silica (>90 wt% Si) phase occurs as discrete grains that are subhedral-anhedral, up to 100 μm in length, and are less terrestrially weathered than the surrounding silicate phases. This phase exhibits smooth surfaces and does not exhibit exsolution features. The other high-silica phase (80–88 wt% Si) is present as <20 μm sized, anhedral inclusions within the interstitial albitic plagioclase. This Si-rich phase is a darker gray color in reflected light compared to the albitic feldspar, but a lighter gray color compared to the Si-rich phase that occurs as discrete grains. These Si-rich inclusions contain about 16 wt% Al₂O₃ (compared to 21 wt% Al₂O₃ in the interstitial plagioclase) and up to 2 wt% FeO, whereas the interstitial plagioclase contains less than 1 wt% FeO. Moreover, the silica-rich phases included in the albitic plagioclase exhibits exsolution features. The silica-rich phases are similar in composition to the silica-rich phases described by Keil and Bischoff (2008).

Bulk Trace Element Compositions

The bulk rock trace element compositions are represented in Table 6 and Fig. 6. The rare earth

Table 3. Average plagioclase compositions of the four studied meteorites.

wt%	NWA 4799		NWA 7214		NWA 7809		NWA 11071	
<i>n</i>	16	1 σ	23	1 σ	8	1 σ	8	1 σ
SiO ₂	67.2	0.7	67.7	0.6	68.6	0.27	68.1	0.57
Al ₂ O ₃	21.1	0.43	20.6	0.30	20.2	0.38	20.4	0.45
FeO	0.50	0.18	b.d.	b.d.	0.18	0.08	0.32	0.35
CaO	1.68	0.44	1.25	0.33	0.71	0.28	0.88	0.34
Na ₂ O	10.5	0.20	10.5	0.13	10.6	0.14	10.6	0.15
K ₂ O	0.62	0.14	0.71	0.09	1.14	0.26	0.99	0.21
Total	101.5	2.1	100.8	1.4	101.4	1.4	101.3	2.1
An	7.87	0.02	5.92	0.02	3.34	0.01	4.14	0.02
Ab	88.7	0.0	90.1	0.0	90.3	0.01	90.3	0.01
Or	3.45	0.01	4.01	0.00	6.39	0.01	5.53	0.01

b.d. = below detection.

Table 4. Average Fe,Ni metal compositions of the four studied meteorites.

wt%	Kamacite				Taenite			
	NWA 7214		NWA 7809		NWA 11071		NWA 11071	
<i>n</i>	28	1 σ	16	1 σ	18	1 σ	3	1 σ
Cu	b.d.	b.d.	b.d.	b.d.	b.d.	b.d.	b.d.	b.d.
P	b.d.	b.d.	b.d.	b.d.	b.d.	b.d.	b.d.	b.d.
Co	0.47	0.02	0.47	0.04	0.47	0.02	0.36	0.08
Ni	5.27	0.20	4.53	0.98	4.56	1.50	22.9	3.14
Si	4.52	0.10	3.58	0.19	3.41	0.19	5.62	0.29
Fe	89.3	0.59	91.1	1.22	90.9	1.66	70.9	3.13
Total	99.5	0.9	99.7	2.4	99.4	3.4	99.8	6.6

b.d. = below detection.

element (REE) profile of both NWA 4799 and NWA 11071 are slightly light REE (LREE) enriched ([La/Lu]_{CI} of 3.5 and 1.9, respectively) with a slight negative Eu anomaly (Eu/Eu* with Eu* = (Sm/Nd)^{1/2} of 0.72 and 0.79, respectively) (Fig. 6). In contrast, NWA 7214 is LREE depleted ([La/Lu]_{CI} = 0.2) with a large negative Eu anomaly (Eu/Eu* = 0.1). The bulk REE pattern of NWA 7214, the only sample here to contain oldhamite, resembles that of this mineral, as it is the major REE carrier in enstatite-rich meteorites (Floss and Crozaz 1993). Northwest Africa 7809 shows a flat REE profile ([La/Lu]_{CI} = 1.05) and a large negative Eu anomaly (Eu/Eu* = 0.3). Other trace elements are variable among the four NWA samples.

Most moderately trace elements are depleted compared to EH and EL chondrites (corresponding to high-Fe and low-Fe enstatite chondrite parent bodies, respectively), except K and Na, which are enriched in NWA 4799 and NWA 11071. These two meteorites show negative Co-Ni anomalies compared to NWA 7214 and NWA 7809, which have positive Co-Ni anomalies. For the other siderophile elements, all of the NWA samples show similar Fe content with varying As

abundances. In addition, NWA 7214 is enriched in Cr compared to EH and EL.

Oxygen Isotopic Compositions

The oxygen isotopic compositions are $\delta^{18}\text{O}$ are $5.756 \pm 0.604\text{‰}$ (NWA 4799), $6.481 \pm 0.770\text{‰}$ (NWA 7809), $5.996 \pm 0.458\text{‰}$ (NWA 7214), and $6.327 \pm 0.848\text{‰}$ (NWA 11071) and $\delta^{17}\text{O}$ are $2.983 \pm 0.302\text{‰}$ (NWA 4799), $3.331 \pm 0.398\text{‰}$ (NWA 7809), $3.120 \pm 0.260\text{‰}$ (NWA 7214), and $3.296 \pm 0.416\text{‰}$ (NWA 11071) (Table 7; Fig. 7). The oxygen isotopic compositions for both $\delta^{18}\text{O}$ and $\delta^{17}\text{O}$ are heterogeneous among individual meteorites. In addition, the three-isotope plot (Fig. 7) shows that all these samples fall on the terrestrial fractionation line (TFL), with $\Delta^{17}\text{O}$ ranging from -0.045 to -0.091‰ (Table 7).

The O isotopic compositions for the four NWA samples are within error of previously published O isotopic compositions (Clayton et al. 1984; Clayton and Mayeda 1996; Miura et al. 2007). However, the mean isotopic compositions are slightly heavier in $\delta^{18}\text{O}$ and $\delta^{17}\text{O}$ than previously reported enstatite chondrites, including impact melts, such as Ilafegh 009 (Clayton et al. 1984; McCoy et al. 1995; Newton et al. 2000) and aubrites (Clayton and Mayeda 1996; Miura et al. 2007; Barrat et al. 2016). Newton et al. (2000) reported a few enstatite chondrites with heavier O isotopic values such as Indarch (EH4), and Grein 002 (EL4-5). The NWA sample $\Delta^{17}\text{O}$ compositions are slightly lighter than the other enstatite-rich meteorites, except the EH values from Newton et al. (2000).

³⁹Ar-⁴⁰Ar Ages

The NWA samples contain ~40–67 vol% of fine- to coarse-grained enstatite with 7–16 vol% interstitial

Table 5. Average sulfide compositions of the four studied meteorites.

wt%	Troilite				Zincian Daubréelite				Manganese Daubréelite				Niningerite		Oldhamite		Caswellsilverite	
	NWA 4799	NWA 7214	NWA 11071	NWA 7809	NWA 11071	NWA 4799	NWA 7809	NWA 7809	NWA 7214	NWA 7214	NWA 7214	NWA 7214	NWA 7214	NWA 7214	NWA 7214	NWA 7214	NWA 7214	
n	5	28	20	16	16	31	10	18	18	58	15	13	15	13	15	13	15	
Fe	61.2	59.1	60.7	60.6	16.5	16.6	16.8	18.8	18.8	16.3	0.27	0.97	0.27	0.19	0.27	0.97	1.81	
Mg	b.d.	b.d.	b.d.	b.d.	b.d.	b.d.	b.d.	b.d.	b.d.	23.7	1.35	b.d.	1.07	1.35	1.35	b.d.	b.d.	
Mn	b.d.	b.d.	b.d.	b.d.	1.12	1.39	0.87	0.73	0.11	10.8	0.51	0.14	0.44	0.51	0.07	0.14	0.09	
Ca	b.d.	b.d.	b.d.	b.d.	b.d.	b.d.	b.d.	b.d.	b.d.	0.90	53.5	b.d.	0.27	53.5	0.5	b.d.	b.d.	
Zn	n.m.	n.m.	n.m.	n.m.	2.04	1.56	1.78	b.d.	b.d.	n.m.	n.m.	n.m.	n.m.	n.m.	n.m.	n.m.	n.m.	
Na	b.d.	b.d.	b.d.	b.d.	b.d.	b.d.	b.d.	0.21	0.13	0.30	0.06	16.1	0.06	0.02	16.1	1.52		
Ti	0.91	1.59	0.76	0.86	0.04	0.04	0.05	0.11	0.20	b.d.	b.d.	0.20	b.d.	b.d.	0.20	0.05		
Cr	0.58	1.07	0.66	0.70	35.7	36.0	36.0	35.2	2.9	0.50	0.02	37.0	0.02	0.02	37.0	0.38		
S	37.4	37.4	37.2	37.3	44.6	44.8	44.8	44.5	0.73	46.3	43.8	45.7	43.8	0.51	45.7	0.84		
Total	100.1	99.2	99.3	99.5	100.0	100.4	100.2	99.5	7.43	98.8	99.5	100.1	99.5	1.54	100.1	4.69		

b.d. = below detection; n.m. = not measured.

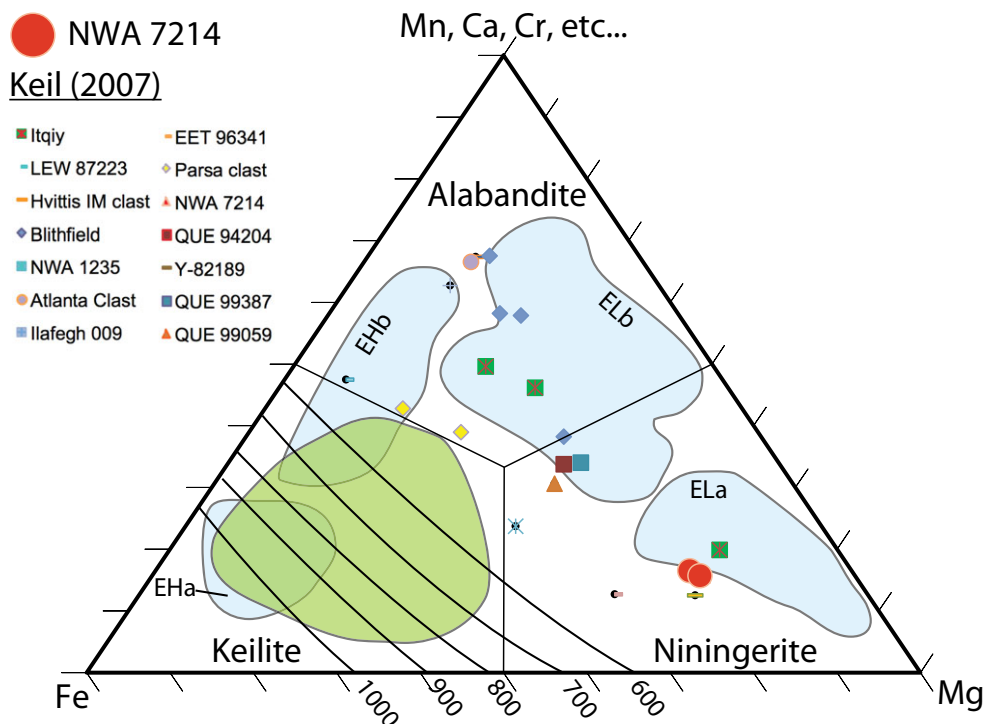


Fig. 5. Ternary diagram of niningerite-alabandite of atomic S based on 1 S for the endmembers Fe, Mg, and Mn + Ca + Cr + all other cations following Keil (2007) and from Skinner and Luce (1971). The only (Mg,Fe,Mn)S phases in NWA 7214 (red dots) are niningerite. Green envelope corresponds to enstatite chondrite impact melts and breccias containing keilite and data points corresponding to enstatite chondrite impact melts and breccias note containing keilite (Keil 2007). Blue envelopes represent the compositions corresponding to the different enstatite chondrite classification from Weyrauch et al. (2018). NWA 7214 falls near the ELa envelope. (Color figure can be viewed at wileyonlinelibrary.com.)

plagioclase (both containing K and Ca). Enstatite does not have a crystal structure that easily accommodates K, so most of the K in this sample is likely to be found in the crystal structure of the plagioclase. The well-defined plateau ages in the mid-temperature steps support this interpretation.

The calculated ^{39}Ar - ^{40}Ar plateau ages for each of the samples investigated range from 4231 ± 6 Ma (NWA 4799, 52 total steps), to 4485.8 ± 1.7 Ma (NWA 7214, 153 total steps), 4489 ± 9 Ma (NWA 7809, 32 total steps), up to 4503.3 ± 3.3 Ma (NWA 11071, 161 steps). ^{39}Ar - ^{40}Ar plateaus and K/Ca ratios are presented in Fig. 8 and Table 8. Plateau ages were calculated assuming a nebular $^{40}\text{Ar}/^{36}\text{Ar}$ value of 1×10^{-4} for the trapped component. The plateau ages of all samples are defined steps ranging 26 for NWA 7809 up to 145 for NWA 7214 and make up >69% of the total $^{39}\text{Ar}_K$ released (Fig. 8; Table 8). In all but one case, the integrated (total fusion) ages are younger than the plateau ages (NWA 4799 = 3954 ± 8 Ma; NWA 7809 = 4410 ± 10 Ma; NWA 11071 = 4449.9 ± 4.5 Ma) due to the first 4.7% to 30% of the total $^{39}\text{Ar}_K$ released that resulted in younger ages (Figs. 8a, 8b, and 8d;

Table 8). In the case of NWA 7214, the integrated age is older by 8.4 m.y. with 4494.2 ± 7.5 Ma. However, the plateau age does not exceed the alpha-95% critical value (15.1 m.y.) so the two ages are analytically indistinguishable from each other (Fig. 8c). The measured atomic K/Ca ratio of the plateau steps vary from ~0.2–0.47 for NWA 4799 and NWA 7214, to 0.2–0.85 for NWA 7809, to ~0.13–0.96 for NWA 11071 over the course of the experiments as different Ar reservoirs are sampled. This indicates that the ^{40}K and $^{40}\text{Ar}^*$ concentrations are homogeneously distributed in the mid- to high-temperature Ar reservoirs in all samples and shows that the samples have not seen any significant high-temperature events after their last crystallization.

The slope of the $^{40}\text{Ar}/^{36}\text{Ar}$ versus $^{39}\text{Ar}/^{36}\text{Ar}$ isochron ages (Figs. 8e and 8f) corresponds to an age of 4220.7 ± 8.8 Ma (NWA 4799), 4484.7 ± 3.5 Ma (NWA 7214), 4464 ± 10 Ma (NWA 7809), and 4499.4 ± 5.0 Ma (NWA 11071) and are consistent with the plateau age at the alpha-95 percent confidence level. For NWA 4799, NWA 7809, and NWA 11071, the first steps do not lie on the linear array defined by the remaining steps (Figs. 8e, 8b, and 8h), which is

Table 6. Bulk major and trace element analyses of the four enstatite chondrite impact melts.

wt%	NWA				BHVO-2 average (<i>n</i> = 6)
	4799	7214	7809	11071	
TiO ₂	0.06	0.14	0.04	0.04	2.71
Al ₂ O ₃	2.34	0.54	1.38	1.73	13.4
FeO	32.9	41.0	29.7	28.3	12.3
MgO	23.5	14.0	20.4	18.5	7.20
CaO	0.62	0.72	0.96	0.45	11.4
Na ₂ O	0.92	0.65	0.66	0.86	2.19
K ₂ O	0.12	0.05	0.09	0.10	0.51
P ₂ O ₅	0.28	0.28	0.14	0.23	0.26
SiO ₂ (calculated)	39.2	42.7	46.6	49.8	50.0
Total	100.0	100.0	100.0	100.0	100.0
ppm					
Li	3.91	0.69	2.25	2.34	5.00
Sc	8.06	2.85	5.75	5.80	32.0
V	55.2	95.7	29.5	35.5	320
Cr	3019	4356	1568	2014	292
Mn	678	1998	1558	756	1533
Co	256	957	579	271	45.0
Ni	4364	16443	9883	4644	120
Cu	38.9	56.6	25.6	30.2	126
Zn	112	0.00	84.0	122	102
Rb	2.27	0.45	1.71	1.88	9.11
Sr	32.5	3.07	24.0	27.7	389
Y	2.18	0.99	1.73	0.81	28.4
Zr	5.33	4.25	3.46	3.26	170
Nb	0.25	0.19	0.12	0.13	18.4
Sn	0.49	0.07	0.41	0.39	1.92
Cs	0.10	0.01	0.08	0.07	0.11
Ba	202	1.43	12.6	78.7	129
La	1.07	0.042	0.273	0.181	14.4
Ce	2.64	0.175	0.731	0.560	37.1
Pr	0.348	0.038	0.102	0.071	5.33
Nd	1.496	0.240	0.500	0.341	24.6
Sm	0.381	0.089	0.127	0.088	6.23
Eu	0.091	0.005	0.015	0.026	2.06
Gd	0.392	0.118	0.206	0.116	6.28
Tb	0.062	0.023	0.040	0.019	0.96
Dy	0.364	0.169	0.264	0.134	5.32
Ho	0.076	0.037	0.060	0.029	1.00
Er	0.211	0.112	0.176	0.079	2.57
Tm	0.034	0.018	0.030	0.014	0.37
Yb	0.208	0.122	0.148	0.076	2.05
Lu	0.031	0.018	0.027	0.014	0.28
Hf	0.179	0.104	0.108	0.120	4.48
Ta	0.028	0.018	0.009	0.011	1.22
Pb	0.506	0.073	0.250	0.272	1.57
Th	0.257	0.013	0.112	0.051	1.25
U	0.202	0.003	0.046	0.176	0.39

b.d. = below detection; n.m. = not measured.

most likely due to some low-temperature terrestrial weathering in these meteorites. The last few steps of NWA 4799 (last two steps) and NWA 11071 (last five

steps) also do not lie on the array and have low signals (Figs. 8e and 8h). These steps have most likely been influenced by the extraction system blanks, and thus have not been used for the age calculations. In contrast, for NWA 7214 (Fig. 8g), all 153 steps define a linear array. For this particular sample, the plateau age, the integrated/total fusion age, and the isochron age are all internally consistent and therefore, represent the most robust age result, with the plateau age representing the best age estimate.

For NWA 11071 and NWA 4799, the array intercepts the *y*-axis at -19.0 ± 5.0 and 19.0 ± 5.4 , respectively, which indicates a $^{40}\text{Ar}/^{36}\text{Ar}$ ratio for the “trapped” component. However, these values for the “trapped” component are not statistically different from the nebular value of 1×10^{-4} . For samples NWA 7214 and NWA 7809, the array intercepts the *y*-axis at -2.47 ± 0.45 and 27.3 ± 9.8 , respectively, indicating a $^{40}\text{Ar}/^{36}\text{Ar}$ ratio for the “trapped” component that is slightly different than the assumed nebular value of 1×10^{-4} . However, the isochron ages are consistent with the plateau ages at the alpha-95% confidence level. This indicates (1) that the “trapped” $^{40}\text{Ar}/^{36}\text{Ar}$ as determined by the isotope correlation diagram does not have a significant impact on the two different methods for calculating an age; and (2) that the $^{39}\text{Ar}_K$ and radiogenic argon are homogeneously distributed within this sample, providing further evidence that this sample has not experienced any major thermal events since crystallization.

DISCUSSION

Reclassification of the NWA Meteorites as Enstatite Chondrite Impact Melts

Using the petrological differences between enstatite-rich meteorite groups, we propose that NWA 4799, NWA 7214, NWA 7809, and NWA 11071, which were formerly classified as aubrites (Meteoritical Bulletin Database #96), represent instead enstatite chondrite impact melts. It is important to note that aubrites do not originate from melted enstatite chondrite parent bodies as shown by their mineralogical differences, including their lower Fe,Ni/troilite ratio, the higher abundances of Ti in troilite, and the presence of diopside and olivine in aubrites, which contrasts with enstatite chondrites (aside from a few exceptions) (Keil 1968; Watters and Prinz 1979; Grossman et al. 1985; Brett and Keil 1986; Kitamura et al. 1987; Okada et al. 1988; Crozaz et al. 2003; Fogel 2005; Lin et al. 2005; McCoy et al. 2018).

Our investigation into the petrological and geochemical nature of these meteorites reveal several lines of evidence that show these meteorites have chondritic,

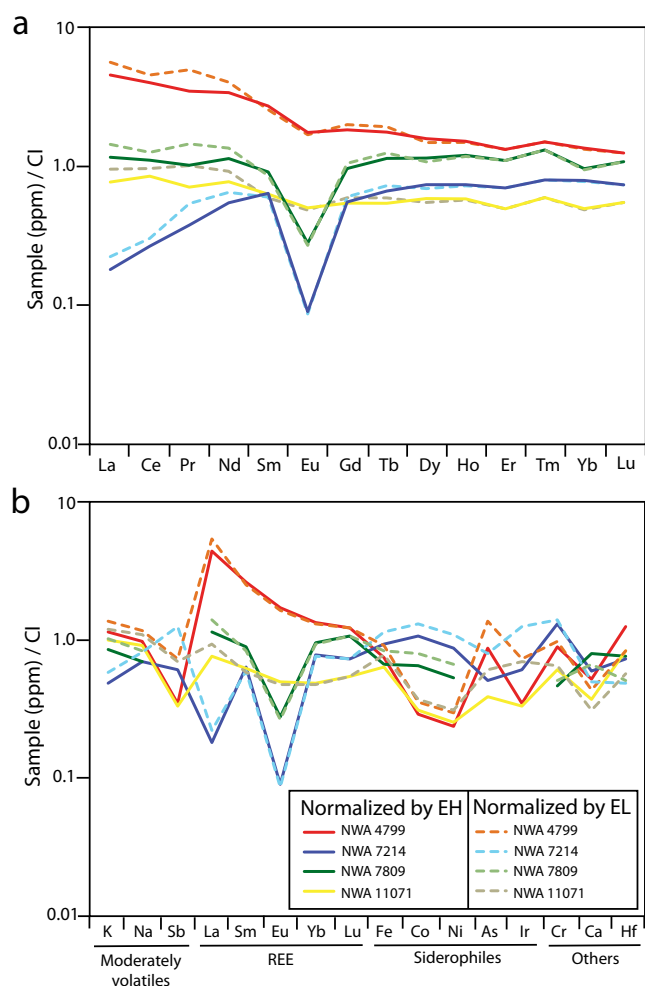


Fig. 6. a) Bulk rock trace element patterns and (b) Bulk rock REE pattern of the four investigated meteorites normalized by bulk EH and EL (Lodders and Fegley 1998). See text for more details. (Color figure can be viewed at wileyonlinelibrary.com.)

and not aubritic, compositions and mineralogies (1) Similar to other impact melt meteorites, the NWA meteorites are almost unfractionated compared to enstatite chondrites (Van Niekerk et al. 2014) as indicated by the relative modal abundances of troilite, metal, and plagioclase of the four studied samples (Table 1). The impact melt samples in Van Niekerk et al. (2014) are more troilite-rich compared to the NWA meteorites in this study, possibly due to the difference in terrestrial alteration of troilite in the NWA meteorites from the present study. In contrast to aubrites, a large amount of pre-terrestrially weathered metal is present in the four NWA meteorites. Formation on a differentiated parent body, such as that of the aubrites, would have effectively segregated metals from silicates, which is observed among aubrites, and is not what is observed in NWA 7214, NWA 7809, and NWA 11071 (Fig. 2). (2)

The dominant silicate phase in the four NWA meteorites is enstatite. Enstatite is the only pyroxene present in all four samples, which is significantly different from what has been reported in aubrite samples. In addition to enstatite, aubrites have diopside (up to 20% in Norton County), as distinct grains and as exsolution lamellae in enstatite (Okada et al. 1988; Keil 1989; McCoy et al. 2018). The lack of diopside in the four investigated samples is in agreement with an affinity to enstatite chondrites, which lack diopside as well, although diopside has been reported in some enstatite chondrites (Kitamura et al. 1987; Floss et al. 2003). In addition, aubrites have forsteritic olivine with modal abundances in the range 0.3–10 vol% (Keil 2010). In particular, Norton County has up to 10 vol% olivine (Watters and Prinz 1979). In contrast, both enstatite chondrites and enstatite chondrite impact melts are typically devoid of olivine. Olivine is also entirely absent from NWA 4799, NWA 7214, NWA 7809, and NWA 11071, further supporting the notion that these samples are more akin to enstatite chondrites rather than aubrites. Note that olivine is found in EL3 and EH3 chondrites in small quantities (Weyrauch et al. 2018). Note that the lack of olivine in these samples point to a E4–6 body as only E3 chondrites contain olivine (Weyrauch et al. 2018). (3) Troilite is only present in NWA 7214, NWA 7809, and NWA 11071, and is Cr- and Ti-bearing. In contrast to the typically Ti-enriched troilite (up to 5.7 wt% Ti) found in aubrites, our samples contain on average 1.1 wt% Ti, with a maximum of 2.5 wt% Ti, which was measured in one grain in NWA 7214 (Watters and Prinz 1979; Brett and Keil 1986). Although the Ti concentrations measured in troilite in NWA 7214, NWA 7809, and NWA 11071 are slightly greater than what is typically observed in enstatite chondrites (0.27–0.77 wt% Ti) (Keil 1968; Weyrauch et al. 2018), they have substantially less Ti in troilite than in aubritic troilite. (4) Fe,Ni metals in the NWA samples contain an average of 4 wt% Si, which differs considerably from the average Si content in aubritic metal of 0.9 wt% (Watters and Prinz 1979). (5) Graphite, observed in the four samples studied here, is commonly found in enstatite chondrites, but not in aubrites (Keil 1968).

With the geochemical affinity to enstatite chondrites established for the four NWA meteorites, we further characterize the type of enstatite chondrite these samples represent. These rocks are not simply high-metamorphosed enstatite chondrites due to the uniform size and distribution of pyroxenes (Figs. 2 and 3) and the lack of 120° triple junctions and relict chondrules. The lack of 120° triple junctions also indicates that these rocks are not primitive enstatite achondrites (Pilski et al. 2011). In addition, the presence of plagioclase suggests that the NWA meteorites are not

Table 7. O isotopic compositions of four investigated samples. Isotopic values in ‰.

Sample	mg	$\delta^{18}\text{O}$	$\delta^{18}\text{O}$ average	1 SD	$\delta^{17}\text{O}$	$\delta^{17}\text{O}$ average	1 SD	$\Delta^{17}\text{O}$	$\Delta^{17}\text{O}$ average	1 SD
NWA 4799	1.2	5.429	6.327	0.77	2.834	3.331	0.398	-0.033	-0.091	0.0099
	1.2	5.384			2.784			-0.059		
	2.4	6.453			3.330			-0.077		
NWA 7809	2.4	7.370	5.756	0.604	3.790	2.983	0.302	-0.101	-0.056	0.022
	1.1	6.002			3.085			-0.084		
	16.0	6.072			3.118			-0.088		
NWA 7214	2.1	6.464	6.327	0.848	3.383	3.296	0.416	-0.030	-0.045	0.042
	1.1	5.977			3.114			-0.042		
	1.6	5.548			2.864			-0.065		
NWA 11071	1.0	7.296	5.996	0.458	3.775	3.12	0.26	-0.078	-0.046	0.018
	1.4	5.720			3.022			0.002		
	1.6	5.966			3.089			-0.061		

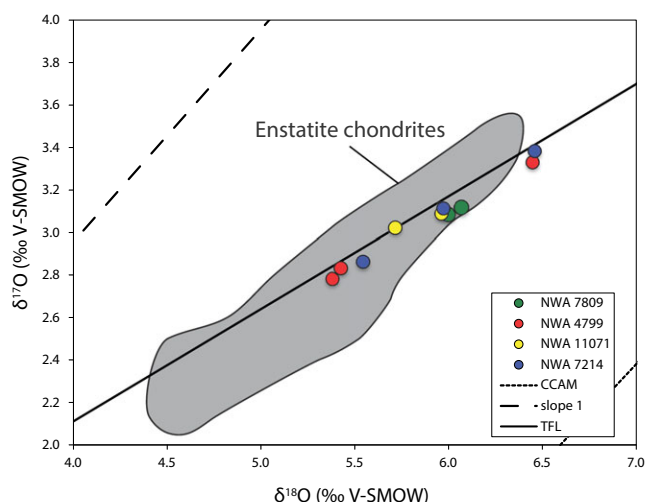


Fig. 7. $\delta^{18}\text{O}$ versus $\delta^{17}\text{O}$ for the four NWA samples including the terrestrial fractionation line (TFL) and enstatite chondrites envelopes from Clayton et al. (1984) and Newton et al. (2000). Errors are smaller than the symbols. CCAM = Carbonaceous chondrite anhydrous mineral line. All NWA samples falls on or slightly below the TFL. V-SMOW = Vienna standard mean ocean water. (Color figure can be viewed at wileyonlinelibrary.com.)

enstatite-rich partial melt residues, such as NWA 2526 and Itqiy (Patzer et al. 2001; Keil and Bischoff 2008). Troilite and metal inclusions in enstatite grains also indicate that these rocks were formed from complete melting similar to the Queen Alexandra Range (QUE) 94204 and paired impact melt rocks and Ilafegh 009, as indicated by troilite and metal inclusions in enstatite grains (McCoy et al. 1995; Van Niekerk et al. 2014). The occurrence of minor silica-phases in enstatite chondrite impact melts is expected as enstatite chondrites contain, although scarce, Si-rich phases (Keil 1968). Happy Canyon also contains glass with compositions similar to those observed in this study (Olsen et al. 1977). In contrast to an internally driven

melting event, several lines of evidence suggest impact histories for these four samples. The presence of troilite or enstatite surrounded by metal suggests that gravitational segregation of metal and sulfide did not occur, indicating rapid melting and subsequent cooling in the four investigated meteorites of this study (Figs. 1 and 2). In addition, the texture of enstatite, which is euhedral and equigranular, in a matrix of plagioclase, metal, and sulfide in the four NWA meteorites (Figs. 2 and 3), likely indicates superheating of the impact melts followed by rapid crystallization, which is evident for impact melting. Pyroxene size, especially in NWA 11071, is finer than what is usually observed in aubrites (up to 5 mm; Keil 2010). Similar textures were observed in the enstatite chondrite impact melt Ilafegh 009 and Happy Canyon (McCoy et al. 1992, 1995). Most enstatite chondrite impact melts consist of euhedral enstatite laths. Euhedral laths of enstatite compared to the subhedral enstatite observed in the studied samples likely indicate a lower nucleation density and slower cooling rate than that of NWA samples, as well as Ilafegh 009 and Happy Canyon. Consequently, the four NWA meteorites likely represent impact melt products of enstatite chondrite precursor material, contrary to their previous classification as aubrites.

Petrogenesis of the NWA Meteorites

Terrestrial Contamination

The four investigated enstatite chondrite impact melts contain various amounts of terrestrial alteration phases. Terrestrial alteration is most evident in the bulk REE compositions of NWA 4799, although alteration is also present in NWA 7809, and NWA 11071, as they are enriched in LREE compared to both EH and EL (Fig. 6). Enrichment of alkali elements in NWA 4799 and NWA 11071 compared to EH and EL could also originate from terrestrial contamination. As described

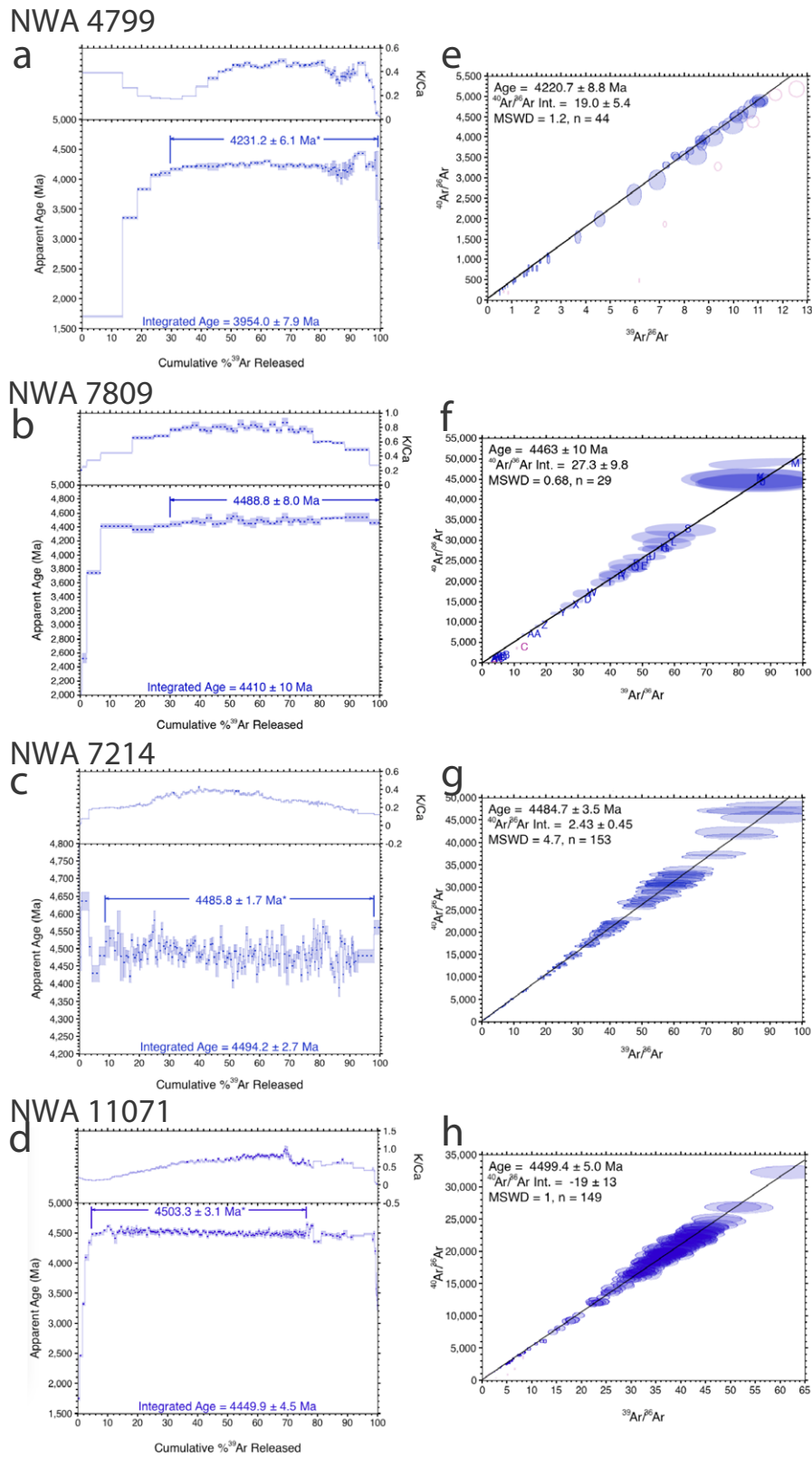


Fig. 8. a–d) ³⁹Ar–⁴⁰Ar ages (Ma) and K/Ca versus cumulative ³⁹Ar% released, individual uncertainties are indicated by the width of the rectangles, and (e–h) isochron plots of ⁴⁰Ar/³⁶Ar versus ³⁹Ar/³⁶Ar for NWA 4799, NWA 7809, NWA 7214, and NWA 11071, respectively. (Color figure can be viewed at wileyonlinelibrary.com.)

Table 8. Ar-Ar plateau and isochron ages for the four NWA meteorites.

Meteorite	Plateau age, Ma (%)	$\pm 1\sigma$ (w/o J)	$\pm 1\sigma$ (w/J)	MSWD	n steps for plateau	Ca/K	$\pm 1\sigma$	Total ^{39}Ar isochron			Integ. age (Ma)	$\pm 1\sigma$	Integ. $40^*/^{39}\text{K}$	$\pm 1\sigma$
								Age (Ma)	Intercept	Intercept				
NWA 4799	4231.1 \pm 6.1 (33.7–99.3)	6.1	6.7	1.7	45	3.751	0.023	4220.7 \pm 8.8	19.0 \pm 5.4	3954.0	7.9	375.5	1.8	
NWA 7809	4488.8 \pm 8.0 (10.1–98.1)	1.7	3.3	2.3	145	4.623	0.009	4463 \pm 10	27.3 \pm 9.8	4494.2	2.7	523.1	0.9	
NWA 7214	4485.8 \pm 1.7 (6.1–76.4)	3.1	4.3	0.9	132	4.480	0.019	4484.7 \pm 3.5	2.43 \pm 0.45	4449.9	4.5	509.2	1.4	
NWA 11071	4503.3 \pm 3.1 (34.1–100)	8.0	8.5	0.6	26	1.917	0.020	4499.4 \pm 5.0	–19 \pm 13	4410.0	10.0	497.2	3.1	

by Stelzner et al. (1999), enrichment in Ba and Sr, as observed in NWA 4799 (202 ppm and 32.5 ppm, respectively) is evidence of terrestrial alteration. The least altered sample, NWA 7214, displays the highest abundance of Ni and Co, which may indicate lower amounts of terrestrial contamination (Stelzner et al. 1999). However, the difference in Ni and Co (including Co-Ni anomalies) might correspond to different abundances of metal in the chips measured for bulk rock analyses.

Metallic and sulfide phases are among the first to weather in hot-desert environments (Van Niekerk et al. 2014), which is particularly problematic for REE abundances given that the primary REE carrier in enstatite-rich meteorites is oldhamite (Floss and Crozaz 1993). The sample NWA 7214 is the least altered and contains the highest modal abundances of metal and sulfides (12–13 vol% and 7.2–7.7 vol%, respectively). Commonly, daubréelite in the four studied meteorites is observed as an exsolution product from troilite; however, some rare individual grains of daubréelite are observed, suggesting that troilite could have been preferentially weathered relative to daubréelite (Fig. 1f). In addition, although the NWA samples show similar textures and modal abundances to the enstatite chondrite impact melt Ilafegh 009 and Happy Canyon (McCoy et al. 1995) (Fig. 3), they contain lower abundances of troilite but higher abundances of terrestrial weathering. This is another indication that terrestrial alteration has considerably affected our samples and has most likely substantially altered troilite leading to lower abundances of this mineral. Ca-rich weathering materials, present in the studied samples, were previously suggested to be alteration products of oldhamite. However, Ca-rich weathering materials and oldhamite are not associated. Thus, it is not clear if the Ca-rich weathering materials formed from oldhamite in the NWA samples.

Cooling History

The four enstatite chondrite impact melts generally have similar grain sizes and textures (Fig. 3), and thus, likely underwent similar petrogenetic histories, although enstatite grain sizes are slightly larger in NWA 11071 and slightly smaller in NWA 4799 compared to the other impact melts. It is important to note that grain size distribution is relatively heterogeneous in these four meteorites likely due to sample bias. Although enstatite chondrite impact melts begin as superheated melts, they undergo rapid crystallization of pyroxene upon cooling. Previous studies have shown that enstatite chondrite impact melts have varying cooling histories after that initial rapid crystallization of enstatite, indicating different burial depths of samples in their parent bodies.

The mineralogical relationships within the NWA samples imply that they underwent slow cooling and reequilibration after crystallization. For example, exsolved schreibersite in Fe,Ni metal and exsolved daubréelite lamellae in troilite are present in the NWA samples, indicating relatively slow cooling regimes, as P and Cr did not remain in their host mineral, and thus exsolved into schreibersite and daubréelite, respectively (McCoy et al. 1995). In order for daubréelite to have exsolved from troilite, as seen in the NWA samples, temperatures lower than 600 °C must have occurred. In addition, slow cooling is indicated by the lack of zoning in plagioclase and niningerite suggesting reequilibration after crystallization. Slow cooling is also implied by exsolutions of troilite in niningerite (Lin and Kimura 1998).

The compositions of (Mg,Fe,Mn)S minerals, such as keilite and niningerite, have been used to constrain postimpact cooling rates of enstatite chondrite impact melts (e.g., Keil 2007). Keilite ($[\text{Fe}_{>50}, \text{Mg}_{<50}]\text{S}$) has been observed in impact melt rocks and breccias as well as enstatite chondrites (Keil 2007; Weyrauch et al. 2018). Keilite is not present in the four enstatite chondrite impact melts of this study (Fig. 6), similar to the anomalous QUE 94204 paired enstatite chondrites (Van Niekerk et al. 2014). Niningerite was observed in this study, however only in NWA 7214. Niningerite forms at temperatures below 500 °C, below the temperature of formation of keilite (>500 °C), suggesting an equilibration temperature at or below 500 °C for the NWA meteorites. It is possible that these rocks were buried after impact, thus keilite could have formed through annealing, and troilite could have formed as an exsolution product of keilite, followed by formation of niningerite. However, the lack of (Mg,Fe,Mn)S phases in all four of the studied samples suggests that cooling history cannot solely be inferred by the presence or absence of keilite due to biased sampling.

Parent Bodies of the Enstatite Chondrite Impact Melts

Similar to ordinary chondrites, enstatite chondrites are divided into two groups, and thus originated from at least two parent bodies, based on their bulk iron contents: high-Fe (EH) and low-Fe (EL) (Sears et al. 1982; Keil 1989; Brearley and Jones 1998). In addition, anomalous enstatite chondrites, such as LaPaz Icefield (LAP) 031220, Lewis Cliff (LEW) 87223, Yamato (Y)-793225, and QUE 94204, likely represent at least four additional enstatite chondrite parent bodies (Zhang et al. 1995; Weisberg et al. 1997; Lin and Kimura 1998; Van Niekerk et al. 2014). Enstatite-rich meteorites, including EH chondrites, EL chondrites, and aubrites, which have previously been shown to originate from at

least three distinct parent bodies, show identical O isotopic compositions (Clayton et al. 1984; Newton et al. 2000; Miura et al. 2007; Barrat et al. 2016). The O isotopic compositions of the studied NWA samples all fall on the TFL and are similar to the previously reported values for EH, EL, and aubrite meteorites (Fig. 7). Thus, O isotopic compositions alone cannot be used to distinguish parent bodies for enstatite-rich meteorites. The four enstatite chondrite impact melt meteorites in this study have slightly heavier O isotopic compositions than the other enstatite-rich meteorites. These samples are “finds” that were collected in hot deserts, thus, terrestrial alteration could have affected their O isotopic compositions, and could explain heavier $\delta^{18}\text{O}$ compositions, as suggested by Newton et al. (2000). However, each sample was pretreated in order to minimize terrestrial alteration effects on these samples. Alternatively, the heavy $\delta^{18}\text{O}$ observed in our NWA samples could be due to the high amount of plagioclase (7–16 mod%), similar to the case of the aubrite Bishopville, which has a high $\delta^{18}\text{O}$ value that was attributed to its plagioclase-rich nature (Keil 2010; Barrat et al. 2016).

In order to further constrain the parent body or bodies of the four enstatite chondrite impact melts of this study, we use the presence and range of compositions of sulfides and metals (Keil 1968; Sears et al. 1982; Lin and Kimura 1998; Lin and El Goresy 2002; Kimura et al. 2005). Metal compositions indicate EH parent body provenance for the four NWA samples: The uniform Ni values seen in schreibersite grains within NWA 7214, NWA 7809, and NWA 11071 are consistent with an EH parent body, as samples derived from an EL parent body contain schreibersite with compositionally variable Ni content (Lin and El Goresy 2002; Patzer et al. 2004). In addition, kamacite in the four samples contains 3.2–4.7 wt% of Si (EH parent body 1.9–3.8 wt%) and 3.5–5.5 wt% of Ni (EH parent body <6 wt%), indicating an affinity with the EH parent body as opposed to the EL parent body (2–4 wt% Si and 2–4 wt% Ni) (Keil 1968; Lin and El Goresy 2002).

A recent study by Weyrauch et al. (2018) expanded the number of parent bodies for enstatite chondrites from two to four, including EHa, EHb, ELa, and ELb. The “a” enstatite chondrite subgroup contains <2 wt% Cr in troilite, <20 wt% Fe in (Mg,Fe,Mn)S, and abundant daubréelite, whereas the “b” subgroup has opposite characteristics. The differences in mineral compositions between the newly distinguished enstatite chondrite parent bodies are likely due to different thermal histories, which occurred during the formation of their parent bodies (Kimura et al. 2017). Subgroups EHa and ELa have likely experienced lower

temperatures than the EHb and ELb, which might have occurred during the formation of the parent body. The presence of daubréelite, the low-Cr content (<2 wt%) in troilite, the low-Fe content (<20 wt%) in (Mg,Fe,Mn)S, and the low-Ni content in metal (<6.5 wt%) in the four NWA meteorites indicate these rocks are part of subgroup “a” (Weyrauch et al. 2018).

Although many mineralogical characteristics point to an EHa origin, some mineral compositions do not show evidence for a specific parent body: The presence of niningerite indicates EH parent body origin, but this mineral was only observed in NWA 7214 (Keil 1968). In addition, alabandite, which represents EL parent body provenance, was not observed in any samples (Keil 1968; McCoy et al. 1995). The presence (or absence) of niningerite versus alabandite might be due to biased sampling, and therefore it is not a good indicator of parent body origin in this study. It is important to note that distinction of parent bodies according to mineral compositions in impact melt rocks has limitations. Keil (1968) and Lin and El Goresy (2002) showed that the occurrence of Mn-poor (<1.10 wt%) and Zn-bearing daubréelite indicates an EH parent body origin, whereas its absence indicates an EL parent body provenance. Only NWA 7809 contains daubréelite with this composition. Daubréelite in NWA 4799 and NWA 11071 contains Mn and Zn, but is Mn-poor, and daubréelite in NWA 7214 does not contain Zn. These discrepancies indicate that, solely based on daubréelite compositions, the NWA meteorites could originate from up to three different bodies that, as of yet, are not represented in the enstatite chondrite suite. Alternatively, Zn and Mn could have been distributed between daubréelite and other Zn-bearing minerals differently than previously reported during an impact event. In addition, the average An content in plagioclase within the four samples ranges from 1.8 to 11.4 mol%, which is intermediate between the EH ($\text{An}_{>3}$) and EL (An_{13-17}) groups (Keil 1968; McCoy et al. 1995; Zhang et al. 1995; Lin and Kimura 1998). Similar to daubréelite composition, plagioclase in the NWA samples indicates a potential separate enstatite chondrite parent body. No other Na- and Ca-bearing minerals were observed in these meteorites, except minor caswellsilverite and oldhamite in NWA 7214 and thus, Na and Ca could not have been exchanged with other minerals during the impact. On the other hand, Na likely volatilized and fractionated during such an impact event on a parent body similar to Ilafegh 009 and Happy Canyon (McCoy et al. 1995). Volatilization is evident through the moderately volatile elements in NWA 7214 and NWA 7809 that show depletion compared to EH and EL. The Ti content in troilite span a large range (0.01–1.6 wt%), with averages from 0.76 wt% to 1.59 wt% (NWA 11071 and NWA 7214, respectively). These abundances

are larger than previously reported in the impact melt Ilafegh 009 (McCoy et al. 1995). For the four NWA meteorites, titanium content might not indicate an EL or EH parent body, but rather indicates that Ti from the parent rock does not only come from troilite in the target rock prior to impact but also comes from other Ti-bearing minerals, such as osbornite (TiN; McCoy et al. 1995). In addition, although not pointing to a specific parent body, the different Co-Ni anomalies for NWA 4799/NWA 11071 and NWA 7214/7809 could indicate two different parent bodies for the four NWA samples.

To summarize, the four NWA samples have mineralogies indicating EHa parent body provenance. Although there is a slight possibility that the NWA enstatite chondrite impact melts might have originated from up to three different parent bodies that were not previously sampled, based on the daubréelite, troilite, and intermediate plagioclase compositions, we suggest that these discrepancies of compositions are due to impact processes.

Impact Ages

McCoy et al. (1995) and Bogard et al. (2010) proposed an early bombardment event in the area of the solar system that enstatite chondrite parent bodies were located, likely in the inner regions of the protoplanetary disk (Kallemeyn and Wasson 1986). This bombardment event occurred around 4.53 Ga, based on ^{39}Ar - ^{40}Ar ages of EL Hvittis, EH Parsa, and EH Abee and both ^{39}Ar - ^{40}Ar and I-Xe ages of the impact breccia Happy Canyon and the aubrite Shallowater, which were all shock-heated (Bogard et al. 2010). The ungrouped meteorite Zaklodzie, which has an enstatite chondrite precursor, was shock melted at 4.50 Ga and the enstatite chondrite impact melt Ilafegh 009, which shows similar textures as the four NWA meteorites, has ^{39}Ar - ^{40}Ar ages of 4.34–4.44 Ga representing resetting during shock metamorphism (McCoy et al. 1995; Bogard et al. 2010). Similar to Zaklodzie, the enstatite chondrite impact melt NWA 11071 has an ^{39}Ar - ^{40}Ar age of 4.50 Ga representing its formation during impact, because ^{39}Ar - ^{40}Ar age should be completely reset during impact (Bogard et al. 2010). Northwest Africa 7809 and NWA 7214 show an indistinguishable age of 4.49 Ga, whereas NWA 4799 has a young ^{39}Ar - ^{40}Ar age of 4.23 Ga. In some enstatite-rich meteorites, younger ^{39}Ar - ^{40}Ar ages were attributed to the effects of the K-bearing sulfide mineral djerfisherite (Bogard et al. 2010); however, this mineral was not present in our samples. The internal consistency of the plateau ages and the isochron ages for all NWA samples (Fig. 8) suggest very robust age results, which could either indicate possibly two different bodies, or one single parent body that experienced at least two

impact events around 4.5 and 4.2 Ga that could correspond to the NWA sample ejection ages. These results suggest that the area of the solar system, where enstatite chondrite parent bodies were located, has undergone regular impact events from early in the history of the solar system (~4.5 Ga) until at least 4.2 Ga, representing younger impact events than previously reported for enstatite-rich meteorite parent body (4.34 Ga; McCoy et al. 1995). In addition, pairing of NWA 7809 and NWA 7214 samples is possible, due to their similar impact ages, as well as their petrography and bulk composition. However, without an available ejection age, their pairing is not definitive.

Enstatite Chondrite Impact Melts as a Petrologic and/or Geochemical Analog for Mercury?

A unique characteristic of all enstatite-rich meteorites is their highly reduced conditions of formation resulting in their depletion in FeO. In addition to enstatite-rich parent bodies, Mercury was shown to have formed under highly reducing conditions as well (McCubbin et al. 2012; Zolotov et al. 2013). The composition of Mercury was not well understood until the arrival of the MESSENGER spacecraft, which launched in 2004 (e.g., Nittler et al. 2011). It orbited Mercury from March 18, 2011, until it made its planned descent into the surface of the planet on April 30, 2015, with a primary goal of investigating the structure of the planet's interior and the unusual conditions under which its magma formed (Solomon et al. 2001). Data from the MESSENGER X-Ray Spectrometer (XRS) and the Gamma Ray and Neutron Spectrometer (GRNS) show that Mercury's surface exhibits a high-S abundance (up to 4 wt%), low-Ti (<0.8 wt%), and low-Fe abundances (<2 wt%) (Nittler et al. 2011; Evans et al. 2012; Starr et al. 2012; Weider et al. 2015). A unique characteristic of Mercury from a geochemical standpoint is the extremely low oxygen fugacity at its surface (IW–7.3 to IW–2.6) and within its interior (~IW–3) compared to Earth, the Moon, and Mars (McCubbin et al. 2012, 2017; Zolotov et al. 2013). Additionally, Mercury exhibits volatile element abundances that are similar to the Earth, as exemplified by K/Th, K/U, and K/Cl ratios (Peplowski et al. 2011, 2012; Evans et al. 2015).

We do not currently have any known mercurian samples in our collections, which when combined with MESSENGER data would provide strong constraints on Mercury's mineralogy, elemental and isotopic composition, and provide insights into its formation and thermochemical evolution. However, data from MESSENGER have facilitated identification of potential petrologic and geochemical analogs of Mercury among our meteorite collections. Any

mercurian meteorite analog should be highly reduced and exhibit some of the unique geochemical characteristics exhibited by the mercurian surface, including elevated S abundances and low-Fe abundances (McCubbin and McCoy 2016). The mineralogy, composition, and low fO_2 found on the mercurian surface are similar to those of igneous enstatite-rich meteorites, such as enstatite chondrite impact melts and aubrites. Although comparisons between Mercury and aubrites have been made previously (Burbine et al. 2002), little effort has been made to evaluate the efficacy of enstatite chondrite impact melts as a petrologic or geochemical analog for Mercury. Here we compare the mineralogy and geochemical compositions of the mercurian surface and interior to enstatite chondrite impact melts, to determine if they could represent an appropriate petrologic or geochemical analog for Mercury.

In addition to its low fO_2 , Mercury's surface is geochemically diverse and can be divided into different terranes based on chemistry and geomorphology (Nittler et al. 2011; Weider et al. 2012, 2015; Peplowski et al. 2015; Vander Kaaden et al. 2017). The most recent study divided the mercurian surface into nine different terranes using bulk compositions and inferred mineralogies derived from the latest data from the MESSENGER XRS and GRNS instruments (Vander Kaaden et al. 2017). These diverse terranes indicate various geochemical reservoirs in the mercurian interior (Weider et al. 2012; Charlier et al. 2013; Vander Kaaden et al. 2017), and a wide array of magma compositions from komatiitic (high-Mg, MgO >18 wt%) to boninitic (high alkali, SiO₂ >52 wt%), including a broad range of SiO₂ (from ~51 to 61 wt%; Vander Kaaden et al. 2017). Based on geochemical modeling and experimental results (Stockstill-Cahill et al. 2012; Charlier et al. 2013; Vander Kaaden and McCubbin 2015, 2016; Namur et al. 2016a, 2016b; McCubbin et al. 2017; Namur and Charlier 2017; Vander Kaaden et al. 2017; McCoy et al. 2018), the mercurian interior is thought to be dominated by albitic plagioclase (NaAlSi₃O₈, 38–58 wt%), enstatite (up to ~37 wt%), diopside (up to 22 wt%), forsteritic olivine (up to 33 wt%), and minor quartz (up to 8 wt%), as well as graphite based on modeling and experiments. In addition, Ca-, Mg-, and Fe-bearing sulfides observed in enstatite-rich meteorites, such as oldhamite (0–0.33 wt%), niningerite (0–3.23 wt%), troilite (1.6–2.7 wt%), and TiS₂ (0–0.64 wt%) are likely present on Mercury and represent, in total, approximately 1.6–6.5 wt% of normative mineralogy of the mercurian surface (Nittler et al. 2011; Weider et al. 2012; Charlier et al. 2013; Zolotov et al. 2013; Namur et al. 2016a; Vander Kaaden and McCubbin 2016; McCubbin et al. 2017;

Namur and Charlier 2017; Vander Kaaden et al. 2017; McCoy et al. 2018).

Based on the inferred mineralogy, oxygen fugacity, and FeO-poor silicate compositions of Mercury surface rocks, the enstatite chondrite impact melt rocks could represent a valuable petrologic and/or geochemical analog to understand igneous processes on Mercury. However, there are a few important differences between Mercury surface materials and enstatite chondrite impact melts that may hinder the use of enstatite chondrite impact melts as a mercurian petrologic analog. For example, the bulk compositions of enstatite chondrite impact melts and the compositions of any individual terrane on Mercury are likely a mismatch because lavas on Mercury formed from partial melting of a differentiated mantle, and enstatite chondrite impact melts have chondritic, undifferentiated bulk compositions. This is best exhibited by the high modal abundance of Fe-rich metallic phases in enstatite chondrites and the low total Fe abundance of Mercury surface materials. Furthermore, the bulk compositions of enstatite chondrite impact melts are a mismatch for the alkali-rich boninitic and komatiitic volcanic rocks on the surface of Mercury (e.g., Vander Kaaden et al. 2017). Nonetheless, there are aspects of enstatite chondrite impact melts that make them a potentially important geochemical analog for Mercury, and we discuss these aspects in the following text.

The bulk compositions of enstatite chondrites have been used in several models for the bulk composition of Mercury (Nittler et al. 2018), so impact melts of enstatite chondrites could provide important insights into the distributions of major, minor, and trace elements between silicate and metal under the highly reducing conditions of differentiation on Mercury. Additionally, there is substantial overlap between the inferred mineralogy of Mercury and the mineralogy of enstatite chondrite impact melts. In particular, enstatite chondrite impact melts have exotic sulfide phases, graphite, albitic plagioclase, Fe-rich Si-bearing metal, and ferromagnesian silicates with low abundances of FeO, all of which are inferred to be present on the surface of Mercury (Nittler et al. 2011; Weider et al. 2012; Charlier et al. 2013; Zolotov et al. 2013; Namur et al. 2016a; Vander Kaaden and McCubbin 2016; McCubbin et al. 2017; Namur and Charlier 2017; Vander Kaaden et al. 2017; McCoy et al. 2018). These mineralogical similarities, when coupled with the similarly reducing conditions, are a primary reason that enstatite chondrite impact melts can yield important information on igneous processes at the surface of Mercury. In particular, the distributions of major, minor, and trace elements among each of the phases in enstatite chondrite

impact melts can be used to infer how elements are distributed among these same phases on the surface of Mercury. This is particularly important given that the geochemical affinities of elements under highly reducing conditions deviate from their typical behavior exhibited under terrestrial oxygen fugacity (Fogel 1997, 2005; McCoy et al. 1999; Malavergne et al. 2007, 2010; Berthet et al. 2009; McCubbin et al. 2012, 2017; Namur et al. 2016b; Vander Kaaden and McCubbin 2016), and experimental data in these highly reducing systems are limited. In fact, the enstatite chondrite impact melts can be used as a point of comparison for experimental studies that aim to use mercurian starting compositions. The distributions of elements in experimental charges run under mercurian conditions can be compared to enstatite chondrite impact melts to assess for similarities and differences in elemental behavior. For example, smelting reactions have been predicted to occur on Mercury through the interaction of graphite and low-FeO silicate melts under low pressure (McCubbin et al. 2017). The presence of graphite in enstatite chondrite impact melts can be used as a natural analog to understand whether or not smelting reactions can be expected to occur, and if so, how much Si is incorporated into the resulting metallic phases. These observations will help to constrain geochemical models for elemental behavior in reduced magmatic systems over a wide range of temperatures and pressures. Finally, the surface of Mercury has experienced impact processes, and impact melt rocks almost certainly comprise at least a portion of Mercury's surface. Consequently, the differences between enstatite chondrites and enstatite chondrite impact melts may represent an important analog for impact processing of surface materials on Mercury because the differences between those two meteorite groups will provide insights into how impact processing affects geological materials under highly reducing conditions. By comparing NWA enstatite chondrite impact melts to the mercurian surface and interior, we infer that the enstatite chondrite impact melts represent imperfect petrologic analogs to the mercurian surface. However, we show that the enstatite chondrite impact melts represent an important geochemical analog for understanding high-temperature processes and elemental distributions on Mercury. Future studies are needed to discern the efficacy of other enstatite-rich meteorite types as petrologic and/or geochemical analogs of Mercury. Although the aubrites seem to represent an excellent spectral analog (Burbine et al. 2002; Keil 2010), detailed comparisons between the petrology and geochemistry of aubrites and the MESSENGER results are still needed.

SUMMARY

Using mineralogical and compositional evidence, we show here that the previously classified NWA aubrites studied here (NWA 4799, NWA 7809, NWA 7214, and NWA 11071) are in fact enstatite chondrite impact melts with affinities to the EHa parent body and possibly originated from up to three different parent bodies:

- These four meteorites crystallized from chondritic melts and are not aubrites, as shown by an equigranular texture of enstatite, high content of metal, absence of diopside and forsterite, low Ti content in troilite, Si-rich Fe,Ni metal, and presence of graphite.
- The four NWA enstatite chondrite impact melts show similar O isotopic compositions to the EH and EL meteorites, and based on their mineral and bulk rock compositions could have an EHa origin. Varying daubréelite compositions, intermediate plagioclase compositions, and varying bulk rock compositions are likely evidence of impact processes. Alternatively, it possibly indicates that the NWA enstatite chondrite impact melts might originate from up to three different parent bodies that were not previously sampled by the enstatite chondrites.
- The Ar-Ar impact ages of the four meteorites ranges from 4.50 to 4.23 Ga which is in conjunction with other enstatite-rich meteorite ages, indicating early onset of impact events and possible frequent impact events until 4 Ga in the region of the solar system, from which enstatite chondrite and aubrite parent bodies were formed.

Although enstatite chondrite impact melts and the alkali-rich boninitic and komatiitic volcanic rocks on the surface of Mercury are mismatched in bulk composition, there is substantial overlap between the inferred mineralogy, oxygen fugacity, and low-FeO bulk composition of Mercury and enstatite chondrite impact melts. Consequently, enstatite chondrite impact melts could represent a valuable geochemical analog to understand igneous processes on Mercury. In particular, the distributions of major, minor, and trace elements among each of the phases in enstatite chondrite impact melts can be used to infer how elements are distributed among these same phases on the surface of Mercury. Understanding elemental behavior at such low fO_2 can help us better understand the geochemistry of Mercury, and offer a better understanding of reduced mineralogy for future mercurian missions, such as BepiColumbo. Moreover, the geochemistry and elemental distributions within enstatite chondrite impact melt meteorites represent important natural petrologic analogs for Mercury to which experimental observations derived

from MESSENGER data on Mercury can be compared.

Acknowledgments—We thank Minghua Ren and Kent Ross for their help with electron microprobe analyses and Shichun Huang for his help with ICP-MS analyses. We would like to thank the reviewers Addi Bischoff and Makoto Kimura for their helpful reviews. We also thank Nicole Lunning for helpful discussions on the topic of the manuscript. This work was partially funded by the UNLV Faculty Opportunity Award to A.U. Support for this research was provided in part by NASA's planetary science research program.

Editorial Handling—Dr. Kevin Righter

REFERENCES

- Baedecker P. A. and Wasson J. T. 1975. Elemental fractionations among enstatite chondrites. *Geochimica et Cosmochimica Acta* 39:735–765.
- Barrat J. A., Greenwood R. C., Keil K., Rouget M. L., Boesenberg J. S., Zanda B., and Franchi I. A. 2016. The origin of aubrites: Evidence from lithophile trace element abundances and oxygen isotope compositions. *Geochimica et Cosmochimica Acta* 192:29–48.
- Berthet S., Malavergne V., and Righter K. 2009. Melting of the Indarch meteorite (EH4 chondrite) at 1 GPa and variable oxygen fugacity: Implications for early planetary differentiation processes. *Geochimica et Cosmochimica Acta* 73:6402–6420.
- Bischoff A., Palme H., Geiger T., and Spettel B. 1992. Mineralogy and chemistry of the EL-chondritic melt rock Ilafegh-009. Proceedings, 23rd Lunar and Planetary Science Conference. pp. 105–1105.
- Bogard D. D., Dixon E. T., and Garrison D. H. 2010. Ar-Ar ages and thermal histories of enstatite meteorites. *Meteoritics & Planetary Science* 45:723–742.
- Brearley A. and Jones A. 1998. Chondritic meteorites. In *Planetary materials*, edited by Papike J. J. Reviews in mineralogy, vol. 26. Washington, D.C.: Mineralogical Society of America. pp. 303–398.
- Brett R. and Keil K. 1986. Enstatite chondrites and enstatite achondrites (aubrites) were not derived from the same parent body. *Earth and Planetary Science Letters* 81:1–6.
- Bunch T. E., Irving A. J., Wittke J. H., and Kuehner S. M. 2008. Zincian breznaitite and other rare minerals in two cumulate-textured aubrites from northwest Africa. 71st Annual Meteoritical Society Meeting. abstract 5309.
- Burbine T. H., McCoy T. J., Nittler L. R., Benedix G. K., Cloutis E. A., and Dickinson T. L. 2002. Spectra of extremely reduced assemblages: Implications for Mercury. *Meteoritics & Planetary Science* 37:1233–1244.
- Carr M. J., Saginor I., Alvarado G. E., Bolge L. L., Lindsay F. N., Milidakis K., Turrin B. D., Feigenson M. D., and Swisher C. C. III. 2007. Element fluxes from the volcanic front of Nicaragua and Costa Rica. *Geophysics, Geochemistry, Geochemistry* 8.
- Charlier B., Grove T. L., and Zuber M. T. 2013. Phase equilibria of ultramafic compositions on Mercury and the origin of the compositional dichotomy. *Earth and Planetary Science Letters* 363:50–60.
- Clayton R. N. and Mayeda T. K. 1996. Oxygen isotope studies of achondrites. *Geochimica et Cosmochimica Acta* 60:1999–2017.
- Clayton R. N., Mayeda T. K., and Rubin A. 1984. Oxygen isotopic composition of enstatite chondrites and aubrites. *Journal of Geophysical Research* 89:C245–C249.
- Crozaz G., Floss C., and Wadhwa M. 2003. Chemical alteration and REE mobilization in meteorites from hot and cold deserts. *Geochimica et Cosmochimica Acta* 67:4727–4741.
- Evans L. G., Peplowski P. N., Rhodes E. A., Lawrence D. J., McCoy T. J., Nittler L. R., Solomon S. C., Sprague A. L., Stockstill-Cahill K. R., Starr R. D., Weider S. Z., Boynton W. V., Hamara D. K., and Goldsten J. O. 2012. Major-element abundances on the surface of Mercury: Results from the MESSENGER Gamma-Ray Spectrometer. *Journal of Geophysical Research: Planets* 117:117.
- Evans L. G., Peplowski P. N., McCubbin F. M., McCoy T. J., Nittler L. R., Zolotov M. Y., Ebel D. S., Lawrence D. J., Starr R. D., Weider S. Z., and Solomon S. C. 2015. Chlorine on the surface of Mercury: MESSENGER gamma-ray measurements and implications for the planet's formation and evolution. *Icarus* 257:417–427.
- Floss C. and Crozaz G. 1993. Heterogeneous REE patterns in oldhamite from aubrites: Their nature and origin. *Geochimica et Cosmochimica Acta* 57:4039–4057.
- Floss C., Fogel R. A., Lin Y., and Kimura M. 2003. Diopside-bearing EL6 EET 90102: Insights from rare earth element distributions. *Geochimica et Cosmochimica Acta* 67:543–555.
- Fogel R. A. 1997. On the significance of diopside and oldhamite in enstatite chondrites and aubrites. *Meteoritics & Planetary Science* 591:577–591.
- Fogel R. A. 2005. Aubrite basalt vitrophyres: The missing basaltic component and high-sulfur silicate melts. *Geochimica et Cosmochimica Acta* 69:1633–1648.
- Grossman J. N., Rubin A. E., Rambaldi E. R., Rajan R. S., and Wasson J. T. 1985. Chondrules in the Qingzhen type-3 enstatite chondrite: Possible precursor components and comparison to ordinary chondrite chondrules. *Geochimica et Cosmochimica Acta* 49:1781–1795.
- Huang S. and Frey F. A. 2003. Trace element abundances of Mauna Kea basalt from phase 2 of the Hawaii Scientific Drilling Project: Petrogenetic implications of correlations with major element content and isotopic ratios. *Geochemistry, Geophysics, Geosystems* 4:8711.
- Jourdan F. and Renne P. R. 2007. Age calibration of the Fish Canyon sanidine 40 Ar/39 Ar dating standard using primary K – Ar standards. *Geochimica et Cosmochimica Acta* 71:387–402.
- Kallemeyn G. W. and Wasson J. T. 1986. Compositions of enstatite (EH3, EH4,5 and EL6) chondrites: Implications regarding their formation. *Geochimica et Cosmochimica Acta* 50:2153–2164.
- Keil K. 1968. Mineralogical and chemical relationships among enstatite chondrites. *Journal of Geophysical Research* 73:6945–6976.
- Keil K. 1989. Enstatite meteorites and their parent bodies. *Meteoritics* 208:195–208.
- Keil K. 2007. Occurrence and origin of keilite, (Fe>0.5, Mg<0.5) S, in enstatite chondrite impact-melt rocks and impact-melt breccias. *Chemie der Erde—Geochemistry* 67:37–54.
- Keil K. 2010. Enstatite achondrite meteorites (aubrites) and the histories of their asteroidal parent bodies. *Chemie der Erde—Geochemistry* 70:295–317.

- Keil K. and Bischoff A. 2008. Northwest Africa 2526: A partial melt residue of enstatite chondrite parentage. *Meteoritics & Planetary Science* 43:1233–1240.
- Kimura M., Weisberg M. K., Lin Y., Suzuki A., Ohtani E., and Okazaki R. 2005. Thermal history of the enstatite chondrites from silica polymorphs. *Meteoritics & Planetary Science* 40:855–868.
- Kimura M., Yamaguchi A., and Miyahara M. 2017. Shock-induced thermal history of an EH3 chondrite, Asuka 10164. *Meteoritics & Planetary Science* 52:24–35.
- Kitamura M., Isobe H., and Watanabe S. 1987. Diopside in chondrules of Yamato-691 (EH3). *Earth and Planetary Science Letters* 691:38–50.
- Kuiper K. F., Deino A., Hilgen F. J., Krijgsman W., Renne P. R., and Wijbrans J. R. 2008. Synchronizing rock clocks. *Science* 320:500–504.
- Lin Y. and El Goresy A. 2002. A comparative study of opaque phases in Qingzhen (EH3) and MacAlpine Hills 88136 (EL3): Representatives of EH and EL parent bodies. *Meteoritics & Planetary Science* 37:577–599.
- Lin Y. and Kimura M. 1998. Petrographical and mineralogical study of new EH melt rocks and a new enstatite chondrite grouplet. *Meteoritics & Planetary Science* 33:501–511.
- Lin Y. T., Guan Y. B., Wang D. D., Kimura M., and Leshin L. A. 2005. Petrogenesis of the new Iherzolitic shergottite Grove Mountains 99027: Constraints of petrography, mineral chemistry, and rare earth elements. *Meteoritics & Planetary Science* 40:1599–1619.
- Lodders K. and Fegley B. Jr. 1998. *The planetary scientist's companion*. Oxford: Oxford University Press. pp 371.
- Malavergne V., Tarrida M., Combes R., Bureau H., Jones J., and Schwandt C. 2007. New high-pressure and high-temperature metal/silicate partitioning of U and Pb: Implications for the cores of the Earth and Mars. *Geochimica et Cosmochimica Acta* 71:2637–2655.
- Malavergne V., Toplis M. J., Berthet S., and Jones J. 2010. Highly reducing conditions during core formation on Mercury: Implications for internal structure and the origin of a magnetic field. *Icarus* 206:199–209.
- Maloy A. K. and Treiman A. H. 2007. Evaluation of image classification routines for determining modal mineralogy of rocks from X-ray maps. *American Mineralogist* 92:1781–1788.
- McCoy T. J., Keil K., Bogard D., Casanova I., and Lindstrom M. M. 1992. Ilafegh 009: A new sample of the diverse suite of enstatite impact melt rocks (abstract). 23rd Lunar and Planetary Science Conference. p. 869.
- McCoy T. J., Keil K., Bogard D. D., Garrison D. H., Casanova I., Lindstrom M. M., Brearley A. J., Kehm K., Nichols R. H. Jr, and Hohenberg C. M. 1995. Origin and history of impact-melt rocks of enstatite chondrite parentage. *Geochimica et Cosmochimica Acta* 59:161–175.
- McCoy T. J., Dickinson T. L., and Lofgren G. E. 1999. Partial melting of the Indarch (EH4) meteorite: A textural, chemical, and phase relations view of melting and melt migration. *Meteoritics & Planetary Science* 34:735–746.
- McCoy T. J., Peplowski P. N., McCubbin F. M., and Weider S. Z. 2018. The geochemical and mineralogical diversity of Mercury. In *Mercury: The View after MESSENGER*, edited by Solomon S. C., Nittler L. R., and Anderson B. J. P. Cambridge, UK: Cambridge University Press. pp. 176–190.
- McCubbin F. M. and McCoy T. J. 2016. Expected geochemical and mineralogical properties of meteorites from Mercury: Inferences from Messenger Data. 79th Annual Meeting of the Meteoritical Society.
- McCubbin F. M., Riner M. A., Vander Kaaden K., and Burkemper L. K. 2012. Is Mercury a volatile-rich planet? *Geophysical Research Letters* 39:1–5.
- McCubbin F. M., Vander Kaaden K. E., Peplowski P. N., Bell A. S., Nittler L. R., Boyce J. W., Evans L. G., Keller L. P., Elardo S. M., and McCoy T. J. 2017. A low O/Si ratio on the surface of Mercury: Evidence for silicon smelting? *Journal of Geophysical Research: Planets* 122:2053–2076.
- Miura Y. N., Hidaka H., Nishiizumi K., and Kusakabe M. 2007. Noble gas and oxygen isotope studies of aubrites: A clue to origin and histories. *Geochimica et Cosmochimica Acta* 71:251–270.
- Namur O., Collinet M., Charlier B., Grove T. L., Holtz F., and McCammon C. 2016a. Melting processes and mantle sources of lavas on Mercury. *Earth and Planetary Science Letters* 439:117–128.
- Namur O., Charlier B., Holtz F., Cartier C., and McCammon C. 2016b. Sulfur solubility in reduced mafic silicate melts: Implications for the speciation and distribution of sulfur on Mercury. *Earth and Planetary Science Letters* 448:102–114.
- Namur O. and Charlier B. 2017. Silicate mineralogy at the surface of Mercury. *Nature Geoscience* 10:9–13.
- Newton J., Franchi I. A., and Pillinger C. T. 2000. The oxygen-isotopic record in enstatite meteorites. *Meteoritics & Planetary Science* 35:689–698.
- Nittler L. R., Starr R. D., Weider S. Z., McCoy T. J., Boynton W. V., Ebel D. S., Ernst C. M., Evans L. G., Goldsten J. O., Hamara D. K., Lawrence D. J., McNutt R. L. Jr, Schlemm C. E. II, Solomon S. C., and Sprague A. L. 2011. The major-element composition of Mercury's surface from MESSENGER X-ray spectrometry. *Science* 333:1847–1850.
- Nittler L. R., Chabot N. L., Grove T. L., and Peplowski P. N. 2018. The chemical composition of Mercury. In *Mercury: The view after MESSENGER*, edited by Solomon S. C., Nittler L. R. and Anderson B. J. Cambridge, UK: Cambridge University Press. pp. 30–51.
- Okada A., Keil K., Taylor G. J., and Newsom H. 1988. Igneous history of the aubrite parent asteroid: Evidence from the Norton County enstatite achondrite. *Meteoritics* 23:59–74.
- Olsen E. J., Bunch T. E., Jarosewich E., Noonan A. F., and Huss G. I. 1977. Happy Canyon—A new type of enstatite achondrite. *Meteoritics* 12:109–123.
- Patzer A., Hill D. H., and Boynton W. V. 2001. Itqiy: A metal-rich enstatite meteorite with achondritic texture. *Meteoritics & Planetary Science* 36:1495–1505.
- Patzer A., Schlüter J., Schultz L., Tarkian M., Hill D. H., and Boynton W. V. 2004. New findings for the equilibrated enstatite chondrite Grein 002. *Meteoritics & Planetary Science* 39:1555–1575.
- Peplowski P. N., Evans L. G., Hauck S. A. II, McCoy T. J., Boynton W. V., Gillis-Davis J. J., Ebel D. S., Goldsten J. O., Hamara D. K., Lawrence D. J., McNutt R. L. Jr, Nittler L. R., Solomon S. C., Rhodes E. A., Sprague A. L., Starr R. D., and Stockstill-Cahill K. R. 2011. Radioactive elements on Mercury's surface from MESSENGER: Implications for the planet's formation and evolution. *Science* 333:1850–1852.

- Peplowski P. N., Lawrence D. J., Rhodes E. A., Sprague A. L., McCoy T. J., Denevi B. W., Evans L. G., Martin Head J. K., Nittler L. R., Solomon S. C., Stockstill-Cahill K. R., and Weider S. Z. 2012. Variations in the abundances of potassium and thorium on the surface of Mercury: Results from the MESSENGER Gamma-Ray Spectrometer. *Journal of Geophysical Research: Planets* 117:E00L04.
- Peplowski P. N., Lawrence D. J., Feldman W. C., Goldsten J. O., Bazell D., Evans L. G., Head J. W., Nittler L. R., Solomon S. C., and Weider S. Z. 2015. Geochemical terranes of Mercury's northern hemisphere as revealed by MESSENGER neutron measurements. *Icarus* 253:346–363.
- Pignatale F. C., Liffman K., Maddison S. T., and Brooks G. 2016. 2D condensation model for the inner Solar Nebula: An enstatite-rich environment. *Monthly Notices of the Royal Astronomical Society* 457:1359–1370.
- Pilski A., Przylibski T. A., and Luszczek K. 2011. Primitive enstatite achondrites. *Meteorites* 2011:9–21.
- Rubin A. E. and Scott E. R. D. 1997. Abee and related EH chondrite impact-melt breccias. *Geochimica et Cosmochimica Acta* 61:425–435.
- Rubin A. E., Scott E. R. D., and Keil K. 1997. Shock metamorphism of enstatite chondrites. *Geochimica et Cosmochimica Acta* 61:847–858.
- Sears D. W., Kallemeyn G. W., and Wasson J. T. 1982. The compositional classification of chondrites: II The enstatite chondrite groups. *Geochimica et Cosmochimica Acta* 46:597–608.
- Sharp Z. D. 1990. A laser-based microanalytical method for the in situ determination of oxygen isotope ratios of silicates and oxides. *Geochimica et Cosmochimica Acta* 54:1353–1357.
- Shukolyukov A. and Lugmair G. W. 2004. Manganese-chromium isotope systematics of enstatite meteorites. *Geochimica et Cosmochimica Acta* 68:2875–2888.
- Skinner B. J. and Luce F. D. 1971. Solid solutions of the type (Ca, Mg, Mn, Fe) S and their use as geothermometers for the enstatite chondrites. *American Mineralogist* 56:1269–1296.
- Solomon S. C., McNutt R. L., Gold R. E., Acuña M. H., Baker D. N., Boynton W. V., Chapman C. R., Cheng A. F., Gloeckler G., Head J. W., Krimigis S. M., McClintock W. E., Murchie S. L., Peale S. J., Phillips R. J., Robinson M., Slavin J. A., Smith D. E., Strom R. G., Trombka J. I., and Zuber M. T. 2001. The MESSENGER mission to Mercury: Scientific objectives and implementation. *Planetary and Space Science* 49:1445–1465.
- Starr R. D., Schriver D., Nittler L. R., Weider S. Z., Byrne P. K., Ho G. C., Rhodes E. A., Schlemm C. E. II, Solomon S. C., and Trávníček P. M. 2012. MESSENGER detection of electron-induced X-ray fluorescence from Mercury's surface. *Journal of Geophysical Research E: Planets* 117:1–19.
- Stelzner T., Heide K., Bischoff A., Weber D., Scherer P., Schultz L., Happel M., Schrön W., Neupert U., Michel R., Clayton R. N., Mayeda T. K., Bonani G., Haidas I., Ivy-Ochs S., and Suter M. 1999. An interdisciplinary study of weathering effects in ordinary chondrites from the Acfer region, Algeria. *Meteoritics & Planetary Science* 34:787–794.
- Stockstill-Cahill K. R., McCoy T. J., Nittler L. R., Weider S. Z., and Hauck S. A. 2012. Magnesium-rich crustal compositions on mercury: Implications for magmatism from petrologic modeling. *Journal of Geophysical Research: Planets* 117:E00L15.
- Turrin B. D., Gutmann J. T., and Swisher C. C. III. 2008. A 13 ± 3 ka age determination of a tholeiite, Pinacate volcanic field, Mexico, and improved methods for $40 \text{ Ar}/39 \text{ Ar}$ dating of young basaltic rocks. *Journal of Volcanology and Geothermal Research* 177:850–859.
- Turrin B. D., Swisher C. C., and Deino A. L. 2010. Mass discrimination monitoring and intercalibration of dual collectors in noble gas mass spectrometer systems. *Geochemistry, Geophysics, Geosystems* 11:1–20.
- Van Niekerk D., Keil K., and Humayun M. 2014. Petrogenesis of anomalous Queen Alexandra Range enstatite meteorites and their relation to enstatite chondrites, primitive enstatite achondrites, and aubrites. *Meteoritics & Planetary Science* 49:295–312.
- Vander Kaaden K. and McCubbin F. M. 2015. Exotic crust formation on Mercury: Consequences of a shallow, FeO-poor mantle. *Journal of Geophysical Research: Planets* 120:195–209.
- Vander Kaaden K. and McCubbin F. M. 2016. The origin of boninites on Mercury: An experimental study of the northern volcanic plains lavas. *Geochimica et Cosmochimica Acta* 173:246–263.
- Vander Kaaden K. E., McCubbin F. M., Nittler L. R., Peplowski P. N., Weider S. Z., Frank E. A., and McCoy T. J. 2017. Geochemistry, mineralogy, and petrology of boninitic and komatiitic rocks on the mercurian surface: Insights into the mercurian mantle. *Icarus* 285:155–168.
- Watters T. R. and Prinz M. 1979. Aubrites—Their origin and relationship to enstatite chondrites. Proceedings, 10th Lunar and Planetary Science Conference. pp. 1073–1093.
- Weider S. Z., Nittler L. R., Starr R. D., McCoy T. J., Stockstill-Cahill K. R., Byrne P. K., Denevi B. W., Head J. W., and Solomon S. C. 2012. Chemical heterogeneity on Mercury's surface revealed by the MESSENGER X-Ray Spectrometer. *Journal of Geophysical Research: Planets* 117:1–15.
- Weider S. Z., Nittler L. R., Starr R. D., Crapster-Pregont E. J., Peplowski P. N., Denevi B. W., Head J. W., Byrne P. K., Hauck S. A. II, Ebel D. S., and Solomon S. C. 2015. Evidence for geochemical terranes on Mercury: Global mapping of major elements with MESSENGER's X-Ray Spectrometer. *Earth and Planetary Science Letters* 416:109–120.
- Weisberg M. K., Fogel R. A., and Prinz M. 1997. Kamacite-enstatite intergrowths in enstatite chondrites. 28th Lunar and Planetary Science Conference. p. 523.
- Weyrauch M., Horstmann M., and Bischoff A. 2018. Chemical variations of sulfides and metal in enstatite chondrites—Introduction of a new classification scheme. *Meteoritics & Planetary Science* 53:394–415.
- Zhang Y., Benoit P. H., and Sears D. W. G. G. 1995. The classification and complex thermal history of the enstatite chondrites. *Journal of Geophysical Research* 100:9417.
- Zolotov M. Y., Sprague A. L., Hauck S. A., Nittler L. R., Solomon S. C., and Weider S. Z. 2013. The redox state, FeO content, and origin of sulfur-rich magmas on Mercury. *Journal of Geophysical Research: Planets* 118:138–146.

SUPPORTING INFORMATION

Additional supporting information may be found in the online version of this article:

Table S1. Detection limits (upper limit in ppm) for elements measured at UNLV and JSC EMPA.

Table S2. Major element compositions of enstatite, feldspar, metal, troilite, daubréelite, niningerite, oldhamite, caswellsilverite, schreibersite, and silica-rich areas/Mg-rich areas.